



**HAL**  
open science

## Experimental investigation of a ns-pulsed argon plasma jet for the fast desorption of weakly volatile organic compounds deposited on glass substrates at variable electric potential

K Gazeli, T Vazquez, G Bauville, N Blin-Simiand, B Bournonville, Stéphane Pasquiers, J Santos Santos Sousa

### ► To cite this version:

K Gazeli, T Vazquez, G Bauville, N Blin-Simiand, B Bournonville, et al.. Experimental investigation of a ns-pulsed argon plasma jet for the fast desorption of weakly volatile organic compounds deposited on glass substrates at variable electric potential. *Journal of Physics D: Applied Physics*, 2020, 53 (47), pp.475202. 10.1088/1361-6463/aba870 . hal-02994953

**HAL Id: hal-02994953**

**<https://hal.science/hal-02994953>**

Submitted on 8 Nov 2020

**HAL** is a multi-disciplinary open access archive for the deposit and dissemination of scientific research documents, whether they are published or not. The documents may come from teaching and research institutions in France or abroad, or from public or private research centers.

L'archive ouverte pluridisciplinaire **HAL**, est destinée au dépôt et à la diffusion de documents scientifiques de niveau recherche, publiés ou non, émanant des établissements d'enseignement et de recherche français ou étrangers, des laboratoires publics ou privés.

ACCEPTED MANUSCRIPT

# Experimental investigation of a ns-pulsed argon plasma jet for the fast desorption of weakly volatile organic compounds deposited on glass substrates at variable electric potential

To cite this article before publication: Kristaq Gazeli *et al* 2020 *J. Phys. D: Appl. Phys.* in press <https://doi.org/10.1088/1361-6463/aba870>

## Manuscript version: Accepted Manuscript

Accepted Manuscript is “the version of the article accepted for publication including all changes made as a result of the peer review process, and which may also include the addition to the article by IOP Publishing of a header, an article ID, a cover sheet and/or an ‘Accepted Manuscript’ watermark, but excluding any other editing, typesetting or other changes made by IOP Publishing and/or its licensors”

This Accepted Manuscript is © 2020 IOP Publishing Ltd.

During the embargo period (the 12 month period from the publication of the Version of Record of this article), the Accepted Manuscript is fully protected by copyright and cannot be reused or reposted elsewhere.

As the Version of Record of this article is going to be / has been published on a subscription basis, this Accepted Manuscript is available for reuse under a CC BY-NC-ND 3.0 licence after the 12 month embargo period.

After the embargo period, everyone is permitted to use copy and redistribute this article for non-commercial purposes only, provided that they adhere to all the terms of the licence <https://creativecommons.org/licenses/by-nc-nd/3.0>

Although reasonable endeavours have been taken to obtain all necessary permissions from third parties to include their copyrighted content within this article, their full citation and copyright line may not be present in this Accepted Manuscript version. Before using any content from this article, please refer to the Version of Record on IOPscience once published for full citation and copyright details, as permissions will likely be required. All third party content is fully copyright protected, unless specifically stated otherwise in the figure caption in the Version of Record.

View the [article online](#) for updates and enhancements.

# Experimental investigation of a ns-pulsed argon plasma jet for the fast desorption of weakly volatile organic compounds deposited on glass substrates at variable electric potential

K. Gazeli, T. Vazquez, G. Bauville, N. Blin-Simiand, B. Bournonville, S. Pasquiers and J. Santos Sousa

Université Paris-Saclay, CNRS, Laboratoire de Physique des Gaz et des Plasmas, 91405 Orsay, France

E-mail : [kristaq.gazeli@u-psud.fr](mailto:kristaq.gazeli@u-psud.fr), [stephane.pasquiers@u-psud.fr](mailto:stephane.pasquiers@u-psud.fr), [joao.santos-sousa@u-psud.fr](mailto:joao.santos-sousa@u-psud.fr)

Keywords: plasma jets, microplasmas, desorption, organic molecules, volatile organic compounds, dielectric surface, TDLAS, metastables, argon, NIR absorption spectroscopy, emission spectroscopy

## ABSTRACT

A ns-pulsed argon atmospheric pressure plasma jet (APPJ) was studied for the fast desorption of weakly volatile organic molecules (bibenzyl) deposited on glass substrates at variable electric potential (floating potential or grounded). The experiments focused particularly on thin resistant bibenzyl films (a large thick bibenzyl deposit was also studied), which are more difficult to be desorbed when using a substrate at a floating-potential. The APPJ was probed by means of high-resolution laser absorption spectroscopy to map the Ar( $1s_5$ ) metastable absolute density (spatially and temporally resolved) at the close vicinity of the glass plate where bibenzyl was deposited. Furthermore, the electrical, optical and thermal features of the APPJ were investigated systematically. In this way, the plasma desorption efficacy on thin resistant bibenzyl deposits was evaluated for the envisaged application, by varying the exposure time of the molecules to the APPJ ( $t_{exp}$ , from 10 s up to 180 s). The obtained results confirm the relatively low desorption efficacy in the case of a floating-potential substrate, which improves to some extent with increasing  $t_{exp}$ . However, when the substrate is grounded, the effect of the plasma becomes much more significant (i.e. much higher desorption efficacy). Besides, contrary to the case of a floating-potential substrate, an almost complete desorption of bibenzyl is achieved for  $t_{exp}=180$  s. Similar effects of the APPJ were recorded on a thick bibenzyl deposit, validating the previous results. For both operating conditions (floating-potential and grounded substrate), the plasma action should be due to the production close to the glass surface of relatively high densities of Ar( $1s_5$ ) (up to  $2 \times 10^{13}$  cm<sup>-3</sup>) and of oxidative species, such as atomic oxygen, hydroxyl radical and ozone. Thermal effects might play a synergistic role only when the substrate is grounded, since relatively high gas and glass-surface temperatures (>60 °C) are reached only in this case. The present results are of interest for public-security applications related to the fast detection of resistant prohibited substances, such as narcotics and explosives.

## I. INTRODUCTION

The potential use of atmospheric pressure plasma jets (APPJs) in surface analysis and processing [1–4], thin film deposition [5], agriculture [6] and biomedicine [7] has led to the need of their characterization in the presence of different targets. Hence, various groups focused on the better understanding of the physical/chemical processes governing the interaction of APPJs with dielectric, liquid, and metallic substrates [2,4,7–15]. APPJs are usually obtained using dielectric barrier discharge (DBD) reactors fed with noble gases (mostly He and Ar) and driven by pulsed or sinusoidal high voltages. The physical mechanism of plasma creation in APPJs is attributed to the generation and propagation of guided streamers [16–18], which are confined in the noble gas channel flowing through a thin dielectric tube and penetrating into the ambient air. As so, electrons and highly reactive species (such as ions, radicals and metastables), electric fields in the order of few tens of kV/cm and radiation (UV-IR) are produced outside the plasma reactor, playing a key role in the aforementioned applications.

Recently, several methodical works provided more insight on the dynamics of He APPJs in contact with distinct targets. In [8], the maximum density of He( $2^3S_1$ ) metastables in a  $\mu$ s-pulsed APPJ was found to increase by up to 10 times when the jet impinged on different dielectric and metallic targets compared to the free jet case (i.e. when no target was placed in front of the APPJ). Eight samples were studied; two of them were dielectrics (PTFE and quartz) and the rest were metals of increasing electrical conductivity (from graphite to Cu). Compared to dielectrics, conductive samples had a much bigger influence on the integrated intensity of the absorption line profile of He( $2^3S_1$ ). The integrated intensity measured with the PTFE sample was  $\sim 2$ ,  $\sim 8$  and  $\sim 10$  times lower than with quartz, graphite, and Cu samples, respectively. Thus, He( $2^3S_1$ ) densities were found to be lower with dielectric samples, and increasingly higher with metals of increasing electrical conductivity. In another work, the presence of a grounded brass substrate in front of a  $\mu$ s-pulsed APPJ resulted in an increase of the spatiotemporal intensity of various emissive species ( $NO_\gamma$ ,  $OH^*$ ,  $N_2(SPS)$ ,  $N_2^+(FNS)$ ,  $O^*$ , etc.) and of the helium metastable density close to the brass surface [9]. Furthermore, the measured densities depended on the distance of the target from the tube orifice. A counter-propagated ionization wave (directed from the brass to the high-voltage electrode), modifying the dynamics of the APPJ, was also observed. It started immediately after the impact on the brass surface of the primary ionization wave, and it was observed for positive and negative voltage polarities. This restrike of the ionization wave was confirmed by other experimental works [10] and simulations [11], both stating that it occurs when the jet impinges on high-permittivity targets (such as liquids and metals). Moreover, the speed of the ionization wave and the electron/ion densities increase in the presence of such targets as compared to dielectrics with low permittivity [11]. On the contrary, a greater spread of the ionization wave on the surface and a deeper penetration of the electric field was observed for dielectric substrates [10–15].

1  
2  
3  
4  
5  
6  
7  
8  
9  
10  
11  
12  
13  
14  
15  
16  
17  
18  
19  
20  
21  
22  
23  
24  
25  
26  
27  
28  
29  
30  
31  
32  
33  
34

For Ar APPJs, numerous works can be found referring mostly to the surface modification of polymeric materials [19–22]. Contrary to He jets, fewer studies focusing on the dynamics of Ar APPJs impinging on substrates have been published so far [2,4,13,23–27]. Among them, the improvement of the stability of a ns-pulsed APPJ when impinging on a floating-potential glass plate was reported lately by our group [2,27]. The placement of the plate (perpendicularly to the gas jet) at a short distance from the nozzle of the dielectric tube allows for the creation of a well reproducible diffuse plasma, instead of filamentary. Moreover, when the angle between the Ar jet and the glass surface is reduced (from 90° to 45°), the spatial extension of the surface ionization wave is strongly modified [2]. Besides, we also reported that the absolute density of Ar( $1s_5$ ) metastables depends on the permittivity of the substrate when maintained at a floating potential, increasing with the permittivity of the plate [4]. Regarding the works published by other groups, the interaction of a kHz sinusoidal Ar APPJ with different metal plates (at floating potential) resulted in a noticeable increase of the intensities of the emission spectra of the APPJ [26]. On top of that, it was found that an rf-driven Ar APPJ does not penetrate into a thin capillary tube (inner diameter=250  $\mu\text{m}$ ) when the tube is maintained at a floating potential; but the placement of a grounded metallic ring downstream of the capillary orifice allows for the jet to penetrate inside the tube [24]. The impact on the features of an Ar APPJ (rf-driven) of a silicon wafer mounted on a grounded metal plate was studied in [28]. A more stable discharge and a higher line-of-sight averaged density of Ar( $1s_5$ ) metastable was measured in respect to the free jet. However, no difference was seen when the wafer was not grounded. Finally, the presence of a grounded metal in front of a ns-pulsed Ar APPJ resulted in the formation of a filament (transient spark), which was displaced spatially when the discharge was turned OFF and ON frequently [25].

35  
36  
37  
38  
39  
40  
41  
42  
43  
44  
45  
46  
47  
48  
49  
50  
51  
52  
53  
54  
55  
56  
57  
58  
59  
60

The aforementioned works reveal clearly that the properties of the target modify drastically the APPJ emission, the axial/radial electric field of the guided streamers and the concentrations of reactive species. Among these species, metastables are involved in various processes occurring during the plasma-target interaction [29]. Their study is, thus, of great interest for many applications, such as those related to the desorption of resistant (i.e. difficult to be detected) prohibited substances from targets [1,30]. These applications combine the unique features of low temperature plasmas (LTP) with mass spectrometry (MS) for the real-time detection of those substances (LTP-MS technique). Indeed, various works claim that the use of plasma jets leads to the desorption (and/or ionization for subsequent detection via mass spectrometry) of narcotics, explosives, chemicals, and pharmaceuticals, among others [1,30-35]. The desorption of resistant compounds from different surfaces can be also achieved with more traditional chemical and thermal ionization techniques [36]. However, these methods require the use of different spray solvents and hot sample-coated filaments (heated to temperatures between 800 and 2000° C), respectively, in order to achieve a desorption/ionization of these substances. On the contrary, the use of LTP allows for a much less fragmentation of the analytes, which can be a great advantage for the fabrication of portable analytical

1  
2  
3 devices. Even if fragmentation is present, LTP offers the ability to adjust it effectively by a simple  
4 modification of plasma parameters, e.g. the axial electric field [31]. Furthermore, the LTP method is  
5 particularly fascinating thanks to its simple and at the same time inexpensive, yet usually robust,  
6 construction. It is not dependent on high purity solvents and it generates mainly easy-to-interpret mass  
7 spectra [1,35]. Besides, LTP-MS can be used for the analysis of large surface areas, while the unique design  
8 of APPJs allows for the extraction of the plasma from the reactor and its use for surface sampling without  
9 significant heating. As compared to other commonly used soft ionization techniques such as electrospray  
10 ionization (ESI) and direct analysis in real time (DART), the LTP probe requires no spray solvents, which  
11 enables it to be a potential ion source for portable mass spectrometers [35]. Finally, its use can be realized  
12 at low gas flow rates and has a minimal sensitivity to the distance and angle of the probe-sample-MS inlet  
13 geometry. This is an advantage over ambient ionization sources like ESI, which use relatively high gas flow  
14 rates and narrow range of angles for the sprayer-surface-inlet configuration to obtain optimum efficiency  
15 [31].

16  
17  
18  
19  
20  
21  
22  
23  
24 In most of the reported studies on the applications of LTP-MS, kHz AC discharges operated in  
25 gases such as He, Ar, N<sub>2</sub> or air are used [1,30-35]. The effectiveness of each plasma on the desorption of  
26 different substances from various surfaces depends on different parameters such as the type of the feed gas  
27 and of the substance to be analyzed, the surface of the material exposed to the APPJ, the reactor  
28 configuration, the power deposited into the plasma, among others [30,31,33]. In what concerns the use of  
29 He and Ar as feed gases, the role of metastable atoms in the corresponding APPJs is particularly significant.  
30 They act as energy reservoirs, contributing significantly to the plasma chemistry. As so, they can be  
31 considered as major players in applications related to the analysis of different surfaces when combining  
32 APPJs with mass spectrometry. In this context, the use of Ar instead of He APPJs might be advantageous  
33 in some cases. This is not only because Ar has a lower cost than He, but also because argon metastables  
34 have almost half the energy of helium metastables, allowing for more delicate surface treatments. In fact,  
35 He metastables, due to their higher internal energy (for instance, 19.8 eV for the 2<sup>3</sup>S<sub>1</sub>), can promote, besides  
36 desorption and ionization, a higher fragmentation of the desorbed molecules prior to their detection [31],  
37 which is undesired as it makes their identification via mass spectrometry more complicated. Moreover,  
38 argon is almost 10 times heavier than helium, and, therefore, when it impinges on a target with the  
39 molecules under analysis, it can easily remove the atmospheric oxygen from the surface of the target.  
40 Hence, the bonding of atmospheric oxygen with the desorbed molecules, which leads to undesired matrix  
41 effects, is limited. The objective, thus, in this kind of applications is not to fragmentate the molecules of  
42 interest, but just to desorb them from the surface with minimum fragmentation and dissociative ionization  
43 in the gas phase. Therefore, besides He APPJs, Ar APPJs have also been tested and, in some cases, proved  
44 to be more effective than He APPJs for the detection of certain explosives (RDX), as little fragmentation  
45  
46  
47  
48  
49  
50  
51  
52  
53  
54  
55  
56  
57  
58  
59  
60

1  
2  
3 and low background emission in the recorded mass spectrum were observed [30]. However, more specific  
4 works are needed to better understand the interaction of Ar APPJs with different substrates and to  
5 discriminate the contribution of Ar metastables to the desorption process. Several reports have been  
6 published on the measurement of the line-of-sight averaged density of Ar( $1s_5$ ) metastable in Ar APPJs  
7 [4,27,28,37–40]. Most of them, though, refer to the free jet case, and only few have studied the effect of the  
8 presence of a target [4,27,28]. To our knowledge, two recent works published by our group [4,27] are the  
9 only investigating the effect of different floating-potential dielectric targets on the absolute density of Ar  
10 metastables in an Ar APPJ. Moreover, the impact of the dielectric material on the desorption of organic  
11 molecules (non-resistant weakly volatile organic compounds) deposited on these targets was also studied  
12 in [4] and a correlation with the production of Ar( $1s_5$ ) metastables was attempted for the first time.  
13 However, the influence of the electric potential of a dielectric target on the absolute density of Ar  
14 metastables produced with a ns-pulsed Ar APPJ and their role on the desorption of resistant weakly volatile  
15 organic compounds has not yet been studied. Both were studied, for the first time, in this work.

16  
17  
18  
19  
20  
21  
22  
23  
24 In the present study, a ns-pulsed Ar APPJ was investigated for the fast desorption of resistant  
25 bibenzyl, an aromatic weakly volatile organic compound. To the best of our knowledge, except our previous  
26 works [2,4], there are no published studies reporting on the efficacy of APPJs on bibenzyl removal from  
27 different surfaces. Furthermore, we are not aware of any work reporting on the application of common  
28 chemical and thermal desorption/ionization methods to remove bibenzyl. Such experiments are of  
29 increasing interest for public security applications like, for instance, the detection of explosives [1,30–35].  
30 As many of these substances contain aromatic rings, bibenzyl can be considered as a model molecule to  
31 study the plasma desorption efficacy. Bibenzyl deposits were placed on a thin (1 mm) glass plate (100×45  
32 mm,  $\epsilon_r \approx 4$ ). The plate was either grounded (a metallic tape made of copper was glued under the plate and  
33 connected directly to the circuit's ground via a metallic wire), or maintained at a floating potential (without  
34 metallic tape nor wire). In ns-pulsed Ar APPJs, the presence of a floating-potential glass plate in front of  
35 the jet allowed for the formation of well diffuse discharges after the passage of the streamer's head [27].  
36 Consequently, tunable diode laser absorption spectroscopy (TDLAS) and Abel inversion methods were  
37 applied for the spatial (axial-radial) and the temporal mapping of the Ar( $1s_5$ ) absolute density. These  
38 experiments are useful for the abovementioned applications because Ar metastables are likely to be  
39 involved in the desorption process. The plasma action on the so-called “fresh deposits” (i.e. prepared and  
40 treated during the same day) was methodically studied in [4]. A high desorption efficacy was revealed  
41 depending on the plasma treatment time. However, preliminary tests on the desorption of a more resistant  
42 bibenzyl deposit (see below for definition) revealed a low desorption efficacy (discussed briefly but not  
43 shown in [4]). Therefore, for the fast desorption of more resistant deposits of weakly volatile organic  
44 compounds, more drastic operating conditions of the APPJ-glass system should be determined. They must  
45  
46  
47  
48  
49  
50  
51  
52  
53  
54  
55  
56  
57  
58  
59  
60

lead to i) the production of relatively high absolute densities of Ar( $1s_5$ ) at the close vicinity of the glass plate (i.e. where resistant deposits are placed), and ii) a much better desorption efficacy as compared to that obtained with a floating-potential glass plate [4]. These goals were achieved in this work by changing the electric potential of the glass plate (i.e. from floating potential to grounded). The obtained results are presented and compared systematically with those of the floating-potential plate. For a detailed comparison, the electrical (voltage-current), optical (wavelength-integrated and -resolved emission) and thermal (gas temperature) characteristics of the discharge, as well as the temperature of the glass plate, were considered.

## II. EXPERIMENTAL SETUP

Figure 1 depicts the experimental setup used for the measurement of the Ar( $1s_5$ ) metastable density and the evaluation of the plasma desorption efficacy on resistant bibenzyl deposits. The plasma was produced by means of a coaxial DBD reactor, which is shown in figure 1(a) (see also [27] for more details). The anode electrode of the reactor (a stainless-steel hollow cylinder) was inserted into a dielectric tube made of quartz (1.7 mm and 4.3 mm inner and outer diameters, respectively) and biased by high-voltage positive pulses of 6 kV in amplitude, 224 ns in FWHM and 20 kHz in frequency (fixed herein). The cathode electrode (a copper foil) was glued outside the tube and grounded directly (no resistor). Argon of high purity (99.999%) at a flow rate of 0.3 l/min (litters per minute) was used as the operating gas. Bibenzyl molecules were prepared and deposited on thin (0.2 mm) glass lamellae (42×42 mm) as described in [2,4]. The lamellae with the molecules were left intact in standard room conditions for three days. During this period, the deposits became drier, adhered more strongly to the lamella's surface, and became more resistant (of interest herein). Then, the lamellae with the bibenzyl deposits were placed on the glass plate (1×100×45 mm,  $\epsilon_r \approx 4$ ) and exposed to the APPJ. The glass plate was placed perpendicularly to the propagation axis of the APPJ at a fixed axial distance ( $z=5$  mm) from the nozzle of the reactor's tube ( $z=0$ ), as it is shown in figure 1(a). The action of the gas flow alone and of the APPJ on the samples was studied for different exposure times ( $t_{exp}=10$  s + 20 s + 30 s + 60 s + 180 s, i.e. 300 s of treatment time in total). After each exposure time, the specimens were analyzed using a high-resolution stereomicroscope (Leica microsystems M165C) equipped with an integrated standalone digital camera (IC80HD).

The electrical signals of the discharge (voltage-current) were monitored continuously by a digital oscilloscope (Lecroy Waverunner 204MXi). This was done by means of a wideband voltage divider (Lecroy PMK-PHV) and a current transformer (Magnetlab CT-B5.0), as shown in figure 1(a). In the case of a grounded glass plate, a current pulse was also recorded through the wire connecting the copper tape glued under the plate and the circuit's ground ( $I_{plate}$ , see below for its description), using a second current transformer (Magnetlab CT-C1.0), also shown in figure 1(a). Furthermore, time-integrated emission spectroscopy was applied for the identification of radiative species, and the estimation of the gas

temperature ( $T_{\text{Gas}}$ ) through the rotational temperature ( $T_{\text{Rot}}$ ) of the OH(A), as explained in [27]. The APPJ light was collected using a wideband optical fiber connected to a high-resolution spectrograph (Princeton Instruments Acton SP 2750, 0.75 m focal length,  $1800 \text{ g mm}^{-1}$  grating blazed at 500 nm) equipped with an ICCD camera (Princeton Instruments PI-MAX3, 140–900 nm). For accurate comparison, spectra are calibrated in terms of wavelength and relative irradiance using adequate calibration lamps. For species identification, the plasma emission was recorded throughout the 5 mm-gap between the reactor's tube and the glass plate, while the evaluation of  $T_{\text{Rot}}$  was performed inside three axial zones (see also section IIIB2). An infrared (IR) camera (FLIR i7) was used to monitor the temperature of the quartz tube ( $T_{\text{Quartz}}$ ) and the glass plate ( $T_{\text{Plate}}$ ) during plasma operation, as explained in [4]. The temperature of the working room ( $T_{\text{Room}}$ ) was also measured using a digital hygrometer/thermometer (Velleman<sup>®</sup> 467 Home, BE).

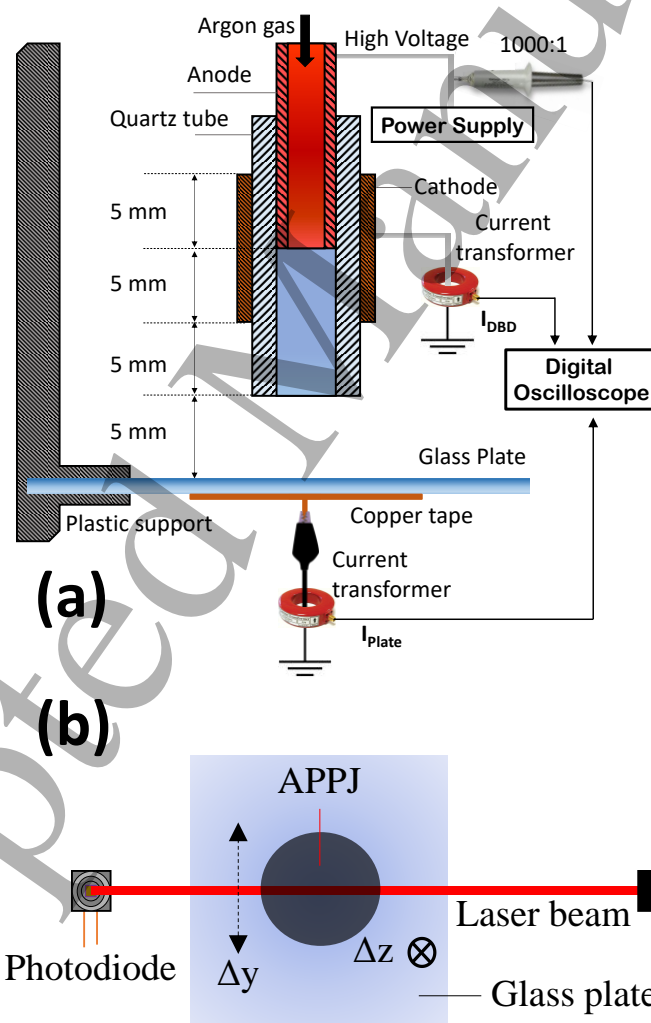


**Figure 1.** (a) Simple scheme of the reactor-plate system and the measurement points of the applied voltage, and of the currents  $I_{\text{DBD}}$  and  $I_{\text{Plate}}$ . The copper tape and the metallic wire under the glass plate are present only in the case of a grounded plate. (b) Simplified sketch of the TDLAS setup used for the measurement of the Ar( $1s_5$ ) metastable absolute density.

Figure 1(b) illustrates a simplified sketch of the TDLAS method used. The plasma was probed by means of high-resolution (spatial and temporal) TDLAS [4,27,37–39]. This method allowed for the accurate mapping of the absolute density of Ar( $1s_5$ ) metastables. The APPJ was traversed by the beam of a continuous laser (Toptica DL 100 DFB-L). Its wavelength was set to that of the radiative transition  $2p_9-1s_5$  of excited Ar (811.531 nm, for more details see [27]). The laser beam was found to be round with a diameter of 18  $\mu\text{m}$  [4] (at the waist), offering a very good spatial resolution. The APPJ-glass plate system was mounted on a 2D micrometric translation stage. In this way, the absorption signal (i.e. the attenuation of the laser beam's intensity due to the production of Ar( $1s_5$ ) in the APPJ) was recorded over the entire APPJ, by translating the APPJ-glass plate system in axial ( $\Delta z$ ) and transversal ( $\Delta y$ ) steps of 0.1-0.5 mm and 0.01 mm, respectively. This was done in the oscilloscope by means of a fast photodiode (New focus 1801, DC-125 MHz, 320-1000 nm). Besides the absorption, three other signals were necessary for the evaluation of the absorbance (obtained via the Beer-Lambert law) [27]. They refer to the emission originating from the APPJ, the background noise, and the laser signal. The absorbance was then used for the determination of the line-of-sight averaged density of Ar( $1s_5$ ), as explained in [27]. The  $\Delta y$  step used was comparable with the beam radius (10  $\mu\text{m}$  versus 9  $\mu\text{m}$ , respectively), and the recorded transversal profiles of the maximum absorbance were well-symmetric around the propagation axis of the guided streamers ( $y=0$ ). In the case of a floating-potential plate, this allowed for the application of the Abel inversion to measure the Ar( $1s_5$ ) absolute radial density [4]. This was also achieved in this work, and it is the first time such has been performed for a ns-pulsed Ar APPJ impinging on a grounded dielectric target. The experimental results shown here focus only on an axial coordinate, in the close vicinity of the plate's surface ( $z=4.8$  mm, i.e. the position of most interest for the envisaged application).

### III. RESULTS AND DISCUSSION

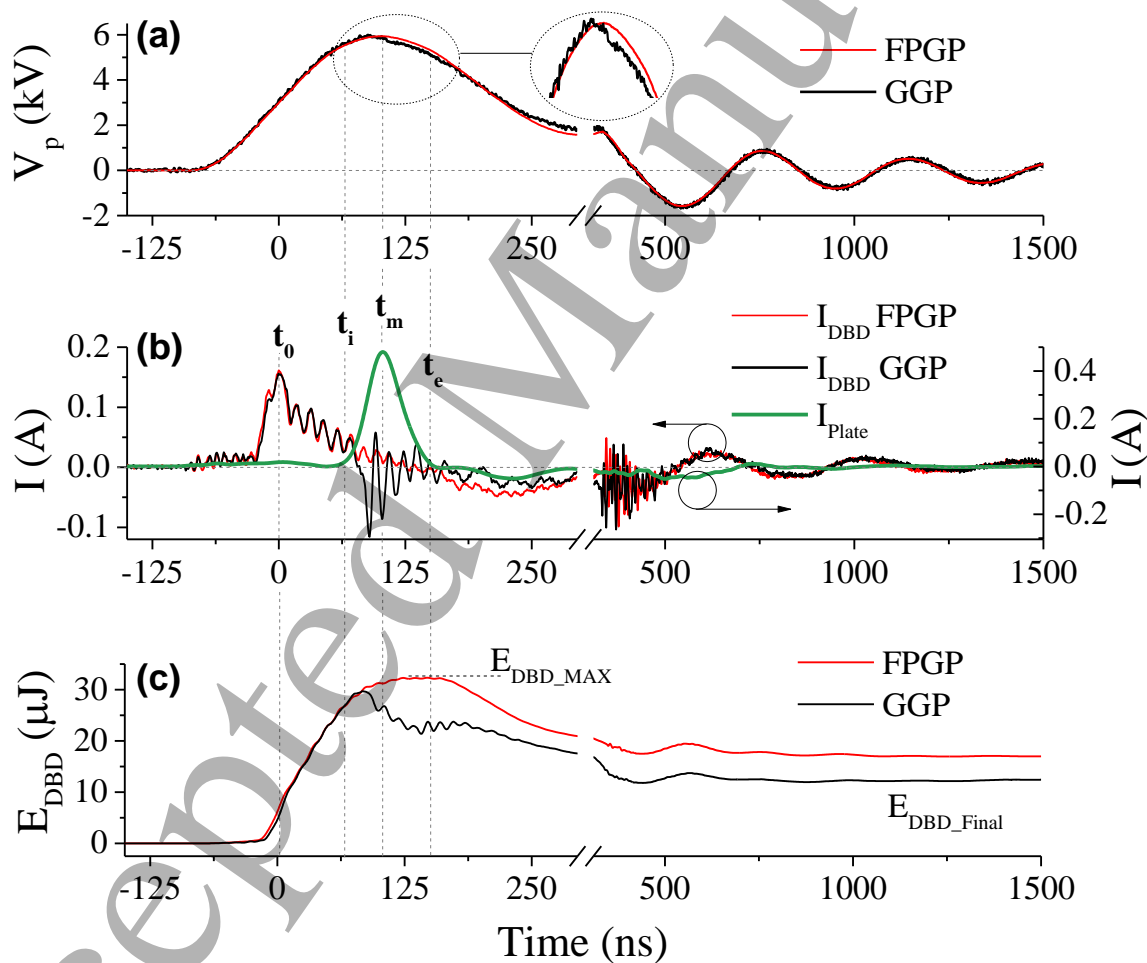
#### A. Electrical characteristics

Figure 2 illustrates electrical signals for the cases of a floating-potential (red) and a grounded (black) glass plates. All sub-figures show average waveforms obtained from 1000 signals in the oscilloscope. The breaks on the time axes are used for a better visualization of the instants  $t_0$ ,  $t_i$ ,  $t_m$  and  $t_e$ . The instant  $t_0$  corresponds to the maximum of  $I_{\text{DBD}}$ , and is set as the origin of time. The plasma strikes on the glass surface at the instant  $t_i$  (~55-60 ns after the instant  $t_0$ ). The instant  $t_m$  (at ~100 ns) corresponds to the maximum of  $I_{\text{Plate}}$ , which is practically zeroed again at the instant  $t_e$  (at ~150 ns). The waveforms of the high voltage delivered to the anode ( $V_p$ , see figure 2(a)) and the DBD conduction current ( $I_{\text{DBD}}$ , see figure 2(b)) are not the same for the two electric potentials of the glass plate. Herein, the term DBD refers to the discharge volume covered by the grounded electrode (copper tape), while the acronym APPJ describes the plasma produced outside the nozzle of the dielectric tube. A detailed description of the method used for the evaluation of the

$I_{DBD}$  can be found in reference [4]. In brief, the applied voltage ( $V_p$ ) and the total current of the DBD (i.e.  $I_{DBD}$  superimposed to the capacitive current ( $I_C$ )) were recorded in the oscilloscope. The gas flow rate was fixed at 0.3 l/min and  $V_p$  was set at the highest value ( $V_{P1} \cong 1.8-1.9$  kV) not causing any plasma ignition. Accordingly, the measured current corresponded to the capacitive current of the DBD. The circuit capacitance ( $C$ ) in our case is 2.3 pF [2], and as it is intrinsic of the system, it does not depend on the applied voltage amplitude. Therefore, the capacitive current at 6 kV was obtained by multiplying the value of  $I_C$  at  $V_{P1}$  with an adequate factor corresponding to the ratio of the two voltages, i.e.  $6/V_{P1}$  ( $\sim 3.1-3.3$ ).  $I_C$  was then subtracted from the total DBD current to obtain  $I_{DBD}$ . For certain representative conditions, three other methods for measuring  $I_C$  were also considered to ensure the reliability of the previous method. Firstly, in some cases, it was possible to measure directly the capacitive current at 6 kV because the plasma did not immediately ignite with the application of the voltage to the anode. Secondly, considering the geometry of the reactor and the permittivity of the dielectric tube,  $C$  was determined based on the theoretical expression of the capacitance of a cylindrical capacitor. Thirdly,  $C$  was measured directly experimentally using an adequate measuring sensor. In cases two and three, the corresponding  $I_C$  at 6 kV was obtained using the expression  $I_C = C \times dV/dt$ , which was then subtracted from the total current to obtain the conduction current ( $I_{DBD}$ ). The  $I_{DBD}$  curves resulting from the four methods were practically the same.

These electrical signals ( $V_p$  and  $I_{DBD}$ ) can be used to obtain the electric power injected into the DBD ( $P_{DBD}$ ), as explained in [4]. By integrating  $P_{DBD}$  over a voltage cycle, the corresponding energy injected into the DBD ( $E_{DBD}$ , see figure 2(c)) was obtained. When the glass plate is maintained at a floating potential, the maximum DBD energy ( $E_{DBD\_MAX}$ , figure 2(c)) is reached shortly after the peak value of the high voltage (around 100 ns in figure 2(a)), and its final value ( $E_{DBD\_final}$ ), at the end of the voltage pulse, is of  $\sim 17$   $\mu$ J.  $E_{DBD\_final}$  is the energy deposited in the DBD over a voltage pulse, and it is relatively higher with a floating-potential plate than with a grounded plate ( $\sim 17$   $\mu$ J versus  $\sim 12$   $\mu$ J, respectively; see figure 2(c)). Note that a drop on the energy waveform for a grounded plate occurs slightly after the instant  $t_i$  ( $\sim 55-60$  ns after  $t_0$ , i.e. when the APPJ strikes on the glass surface). Similarly, a drop of the corresponding high-voltage peak (see inset in figure 2(a)) is measured after  $t_i$ , and the current pulse  $I_{Plate}$  begins to form. Its peak value appears displaced in time as compared to that of the  $I_{DBD}$ . In fact,  $I_{DBD}$  is measured at the cathode, while  $I_{Plate}$  is measured in the wire connecting to the circuit's ground the circular copper tape glued under the glass plate, which is placed at a distance of 10 mm downwards from the end of the grounded electrode (cathode, see figure 1(a)). As so,  $I_{DBD}$  starts as the plasma forms within the DBD volume. At this instant, the APPJ has not yet reached the glass plate.  $I_{Plate}$  begins to form only after the impingement of the streamer's head on the glass plate, which happens at  $t_i$ , several 10s of ns ( $\sim 55-60$  ns) after the instant of the peak of  $I_{DBD}$  ( $t_0$ ). Therefore,  $I_{Plate}$  does not appear during the rise time of the voltage, as it is the case of  $I_{DBD}$ . Different works measuring the current  $I_{Plate}$  in APPJs impinging on various targets can be found in the literature [8,9,25,41].

For instance, in [41], an argon APPJ impinging on a copper target placed 10 mm away from the tube's nozzle was studied. As in our case, the current measured through the voltage drop on a resistor positioned under the target only develops after the rise time of the applied high-voltage pulse. Similar results are presented in [8], concerning a helium APPJ impinging on various targets of increasing electrical conductivity. As another example, a helium APPJ interacting with a metallic target was studied in [9].  $I_{\text{Plate}}$  was measured across a 100 Ohm resistor placed below the target. During the rise time of the voltage,  $I_{\text{Plate}}$  exhibited a slow increase with very low amplitude, but it increased sharply after the voltage rise time, when the APPJ hit the target. This sharp increase after the rise time of the voltage is similar to that of  $I_{\text{Plate}}$  in figure 2(b), which is established after the impact of the streamer's head on the glass target.



**Figure 2.** (a) Applied voltage ( $V_p$ ), (b) conduction current of the DBD ( $I_{\text{DBD}}$ ), and total current recorded through the wire connecting the tape glued under the glass plate and the circuit's ground when the plate is grounded ( $I_{\text{Plate}}$ -green), and (c) energy of the DBD ( $E_{\text{DBD}}$ ) over a voltage pulse, for the cases of a floating-potential (FPGP, red) and a grounded (GGP, black) glass plates.

1  
2  
3 The form of the current  $I_{\text{plate}}$  shown in figure 2(b) is like that reported in [25], and its peak is  
4 noticeably higher than that of  $I_{\text{DBD}}$ . However, it decreases drastically with decreasing voltage amplitude  
5 (for instance, it drops down to  $\sim 0.12$  A at 5 kV (not shown here) from  $\sim 0.45$  A at 6 kV (see figure 2(b))),  
6 which is consistent with the corresponding decrease of almost fourfold of  $I_{\text{DBD}}$  (not shown here). In [25],  
7 the impingement of the jet on a grounded metal produced a plasma filament (transient spark), which  
8 changed drastically the voltage across the gap. This is similar to our work where a thin conductive plasma  
9 channel ( $\sim 700$   $\mu\text{m}$  in diameter) is established between the tube's nozzle and the grounded glass plate after  
10 the impingement of the streamer's head (see figure 3).  $I_{\text{plate}}$  starts to form with the establishment of the  
11 conductive channel, leading to a drop of the applied voltage (see inset in figure 2(a)). However, the voltage  
12 drop reported in figure 2(a) is not as drastic as that in [25]; in fact,  $I_{\text{plate}}$  is  $\sim 10$  times lower in our case, and  
13 we do not observe the formation of a transient spark. This difference is attributed to the following reasons:  
14 i) different voltage pulse features, ii) use of a grounded dielectric instead of a metallic target and iii)  
15 different distance of targets from the tube's nozzle, between our work and [25]. According to [42], the  
16 discharge transitions to the transient glow mode when the streamer bridges the gap and the current rises  
17 sharply. This should be also the case under our experimental conditions. Indeed, in [42], where a He (95%)  
18 / Ar (5%) APPJ impinging on a grounded Teflon film (254  $\mu\text{m}$  thickness) was studied, for a distance of 20  
19 mm between the target and the tube's nozzle, the measured current reached a peak value of  $\sim 0.4$  A, which  
20 is very close to the measured maximum amplitude of  $I_{\text{plate}}$  in our case (i.e.  $\sim 0.45$  A in figure 2(b)). However,  
21 when the distance of the target and its thickness were decreased (to 9 mm and 50.8  $\mu\text{m}$ , respectively) in  
22 [42], the peak current increased up to  $\sim 2.5$  and  $\sim 3.5$  A, respectively. The measured current at 9 mm for the  
23 thicker plate in [42] is 5.5 times higher than in our case. This difference is attributed i) to the much thicker  
24 glass plate used in our work (about 5 times thicker, leading to a lower peak current as suggested in [42])  
25 and ii) to the higher amplitude of the voltage pulse used in [42] (2 times higher). At atmospheric pressure  
26 conditions, the conductivity of the thin argon plasma channel can be estimated using the following equation  
27 [43]:  
28  
29

$$\sigma \approx 0.69 \times 10^{-16} \times n_e \text{ cm}^2 \text{ Ohm}^{-1}$$

30 In our case, the electron density,  $n_e$ , is expected to be in the order of  $\sim 10^{14} \text{ cm}^{-3}$  [44]. Applying this value  
31 to the previous equation,  $\sigma = 0.69 \times 10^{-2} \text{ Ohm}^{-1} \text{ cm}^{-1}$ . The current of the conductive channel can be, thus,  
32 estimated using the following equation [43]:  
33  
34

$$I = \pi \times \sigma \times E \times r_c^2$$

35 where  $E$  is the electric field magnitude in the conductive channel (assumed to be around 20 kV/cm under  
36 our conditions [45]) and  $r_c$  is the radius of the channel ( $\sim 350$   $\mu\text{m}$  from figure 3). Using these values of  $\sigma$ ,  $E$   
37 and  $r_c$ ,  $I \approx 0.53$  A, which is quite close to the measured peak of  $I_{\text{plate}}$  of  $\sim 0.45$  A in figure 2. Note that the  
38  
39  
40  
41  
42  
43  
44  
45  
46  
47  
48  
49  
50  
51  
52  
53  
54  
55  
56  
57  
58  
59  
60

1  
2  
3 values of  $n_e$  and  $E$  were not accurately measured in this work, which induces an uncertainty on the calculated  
4 value of  $I$ .  
5

6 The value of  $I_{\text{Plate}}$  should be proportional to the amount of electrical charges deposited on the glass  
7 plate. When enough electrical charge is deposited on the glass surface, electric fields are sufficiently high  
8 for the initialization of a surface ionization wave (see figure 3). The deposition of electrical charges on the  
9 glass surface can be strongly modified by the placement of the metallic tape under the glass plate, which  
10 can enhance locally the electrical charges adsorption and strongly modify the ionization wave propagation  
11 [46]. Electrical charge deposition happens fast in our case, as it can be deduced from the rise time and  
12 FWHM of the measured  $I_{\text{Plate}}$  pulse ( $\sim 25$  ns and  $\sim 40$  ns, respectively; see figure 2(b)). The amount of  
13 deposited electrical charge can be estimated through the integral of  $I_{\text{Plate}}$  between the instants  $t_i$  and  $t_e$  in  
14 figure 2(b), and it was found to be of 19 nC. In [47], where a kHz AC He APPJ impinging on a grounded  
15 polystyrene petri dish ( $\epsilon_r=2.4$ ) was studied, the amount of electrical charge transferred to the target's surface  
16 was calculated using Lissajous cycles. It was observed that the diameter of the grounded electrode ( $D_{\text{Ground}}$ )  
17 placed under the target affected the total deposited electrical charge. By increasing  $D_{\text{Ground}}$  from 10 to 80  
18 mm, the mean total electrical charge transferred to the target during the positive voltage cycle was increased  
19 from  $5.6 \pm 0.2$  to  $17.5 \pm 0.8$  nC, respectively. These values are  $\sim 3.4$  and  $\sim 1.1$  times lower than that obtained  
20 in our case for a  $D_{\text{Ground}}$  of  $\sim 18$  mm, respectively. Furthermore, in our case, the average electrical charge  
21 density corresponding to the maximum propagation distance of the surface ionization wave (13 mm, instant  
22  $t_e$ , see figure 3(c4)) is of  $14.32$  nC cm $^{-2}$ . This value is quite close to that of reference [48] ( $19.35$  nC cm $^{-2}$ ,  
23 according to our estimations considering a total deposited electrical charge of 950 pC and a maximum  
24 surface ionization wave extension of 2.5 mm, which were reported in [48]). Note that the amount of  
25 electrical charge deposited on dielectric targets by APPJs depends on various factors such as the electric  
26 potential, conductivity and distance of the target from the APPJ's tube outlet, the operating gas and its flow  
27 rate, the excitation voltage waveform and amplitude, and the reactor configuration [47,48].  
28  
29  
30  
31  
32  
33  
34  
35  
36  
37  
38  
39  
40

41 During the current pulse of  $I_{\text{Plate}}$ , noticeable differences on the DBD current waveform ( $I_{\text{DBD}}$ ),  
42 between the use of a grounded and a floating-potential plate, are recorded (see figure 2(b)). Indeed, between  
43  $t_i$  and  $t_e$  (at  $\sim 150$  ns in figure 2(b), end of the  $I_{\text{Plate}}$  pulse, when  $I_{\text{Plate}}$  is again practically zeroed),  $I_{\text{DBD}}$  is  
44 approximately zero in the case of a floating-potential plate, while for a grounded plate, a significant  
45 inversion of the  $I_{\text{DBD}}$  is observed, reaching a maximum negative value of  $-0.12$  A, followed by several  
46 oscillations up to the instant  $t_e$ . The negative current peak of the  $I_{\text{DBD}}$  for a grounded plate is attained slightly  
47 before the instant of the maximum of the  $I_{\text{Plate}}$  ( $t_m$  in figure 2(b), around 100 ns). Note that the waveforms  
48 of figure 2 are average values of 1000 signals in the oscilloscope. The fluctuation of the electrical signals  
49 in the case of a grounded plate is relatively higher than that corresponding to a floating-potential plate. It is  
50 worth to notice that after the  $I_{\text{Plate}}$  pulse (i.e. for  $t > t_e$ ), the temporal evolution of  $E_{\text{DBD}}$  is quite similar for both  
51  
52  
53  
54  
55  
56  
57  
58  
59  
60

1  
2  
3 electric potential conditions of the glass plate (see figure 2(c)). The lower energy values of the DBD over  
4 a voltage cycle when the plate is connected to the ground are, thus, due to a decrease of the applied high  
5 voltage and the inversion of the  $I_{\text{DBD}}$  occurring during the  $I_{\text{Plate}}$  pulse (i.e. between the instants  $t_i$  and  $t_e$ ).  
6  
7

8 The above-mentioned drop of the applied voltage and the inversion of the DBD current when using  
9 a grounded plate denote that a higher current is dragged by the APPJ. This coincides well with the instant  
10 of the formation of the current  $I_{\text{Plate}}$  in figure 2(b). An increase of the APPJ current implies that more  
11 electrons are available in the gas channel for ionization and excitation when using a grounded glass plate.  
12 This is the result of a higher axial electric field and the formation of a more conductive channel in the gas  
13 gap when the glass plate is grounded [49]. Consequently, as stated previously, enhanced  
14 ionization/excitation is expected to happen in the APPJ volume ( $0 \leq z \leq 5$  mm and  $-0.5 \leq y \leq 0.5$  mm) when  
15 using a grounded glass plate. This fact is qualitatively supported by the high-definition photographs of  
16 figure 3(a). Indeed, the APPJ and the subsequent surface ionization wave exhibit brighter emission patterns  
17 for the grounded glass plate. These findings agree with the results obtained using a He plasma jet in a  
18 similar configuration [49]. This is further discussed later in the paper through the analysis of the  
19 wavelength-integrated and -resolved emission of the APPJ.  
20  
21  
22  
23  
24  
25  
26

27 Contrary to the DBD, the energy deposited into the APPJ is not known. The energy delivered to  
28 the reactor by the power supply is not the same between using a floating-potential and a grounded glass  
29 plate (see figure 2). The reactor is driven by a pure voltage (and not a current) generator. Therefore, the  
30 drawn energy is defined by the current that is dragged by a load coupled to the power supply. Under our  
31 experimental conditions, the impedance of the target is expected to change when it is grounded. Therefore,  
32 the load in this case (i.e. DBD + APPJ + glass plate + copper tape + grounded metallic wire) is different  
33 from that in the case of a floating-potential plate (i.e. DBD + APPJ + glass plate). When the plate is at a  
34 floating-potential, the APPJ is in contact with a capacitive load (glass plate) and the ambient atmosphere  
35 (minimal conductivity). For the grounded plate, though, the placement under the thin glass plate of a  
36 metallic tape (connected to the ground via a metallic wire) implies a RC load. Therefore, the closed electric  
37 circuit is different between using a grounded and a floating-potential plate. In other words, the additional  
38 ground-line in the case of a grounded plate affects the  $I_{\text{DBD}}$  current. The differences in  $I_{\text{DBD}}$  between the two  
39 electric potential conditions of the glass plate seen in figure 2(b) are like those reported in [50]. In that  
40 study, the authors investigated the electrical features of an AC kHz Ar plasma jet impinging on metallic  
41 targets of increasing thermal conductivity (from Ti to Cu), which were grounded or maintained at a floating  
42 potential. They measured the power-line current with and without plasma ( $I_{\text{PP}}$  and  $I_{\text{PWP}}$ , respectively), and  
43 they obtained the plasma current by subtracting  $I_{\text{PWP}}$  from  $I_{\text{PP}}$ , i.e. the same method used in our case for  
44 obtaining  $I_{\text{DBD}}$ . Their results revealed that, independently of the target material, the time-averaged plasma  
45 plume current was 3 times higher in the case of the grounded targets as compared to that of the floating-  
46  
47  
48  
49  
50  
51  
52  
53  
54  
55  
56  
57  
58  
59  
60

1  
2  
3 potential targets. This is similar to our work, where a significant inversion of  $I_{\text{DBD}}$  is only recorded for a  
4 grounded plate following the impingement of the APPJ on the glass surface.  
5

6 Even if the current  $I_{\text{plate}}$  is measured, the current in the APPJ volume is not known, which would  
7 allow for a reliable evaluation of the energy deposited into the APPJ. For an accurate measurement of the  
8 APPJ current, a more detailed electrical study needs to be performed, as those reported in [25,51]. However,  
9 this requires a modification of the geometry of our reactor, which is out of the scope of the present study.  
10  
11  
12

## 13 **B. APPJ emission characteristics and absorption spectroscopy analysis**

### 14 ***1. IR and ICCD imaging***

15  
16 Figure 3(a) shows high-definition photos (wavelength- and time-integrated) of the APPJ impinging on a  
17 floating-potential (left) and a grounded (right) glass plates. Guided streamers were produced inside the  
18 dielectric tube and propagated fast towards the glass plate following the path of the gas jet. For the case of  
19 a floating-potential plate, the propagation velocity of the guided streamers was previously measured by our  
20 group, and it was found to be in the order of  $10^5$  m/s [2,27]. It takes, thus,  $\sim 30$  ns for the streamer's head to  
21 reach the glass surface after exiting the dielectric tube, creating behind it a highly conductive ionized  
22 channel which connects the powered electrode and the target. Right after the strike of the streamer's head  
23 on the surface, a bright spot is formed at the contact point, and surface ionization waves (see the  
24 characteristic luminous "disks" in both images) are initiated and spread around the bright spot. The diameter  
25 of the area covered by the surface ionization wave on a floating-potential plate was evaluated using ICCD  
26 imaging, and it reached values up to 10.4 mm [27]. The spreading phenomenon of the surface ionization  
27 wave observed in figure 3(a) is similar to those reported in He APPJs impinging on floating-potential  
28 dielectric targets [10,11,48,52]. According to the literature, electrical charge accumulation on the dielectric  
29 surface leads to the formation of an axial electric field, which opposes and negates that of the streamer. The  
30 axial propagation of the streamer stops, and the radial component of the electric field becomes dominant  
31 [15]. The use of dielectric targets instead of liquids and metals favors, thus, the development of surface  
32 ionization waves and the deeper penetration of the electric field in the material [11,13–15].  
33  
34  
35  
36  
37  
38  
39  
40  
41  
42  
43

44 The high-definition photos shown in figure 3(a) reveal further that when the dielectric target is  
45 directly grounded, the Ar APPJ, the bright spot, and the surface ionization wave become brighter and wider  
46 (compare left and right parts of the figure). This is probably due to an enhancement of the electric field and  
47 the formation of a more conductive channel between the high-voltage electrode inside the tube and the  
48 grounded glass plate. To verify this assumption, the propagation velocity of the streamer in the case of a  
49 grounded glass plate was measured based on the ICCD images of figure 3(c). It was found to be  $\sim 5 \times 10^5$   
50 m/s. This value is  $\sim 2.5$  times higher than that measured in the case of a floating-potential plate [27]. This  
51 finding agrees with the results of reference [45], where the interaction of a ns-pulsed He APPJ with  
52  
53  
54  
55  
56  
57  
58  
59  
60

1  
2  
3 dielectric and metallic targets was investigated both experimentally and numerically. The simulated  
4 electron impact ionization source and electron density, as well as the simulated velocity and electric field  
5 of the ionization wave were higher for the grounded metal target. The electric field is, thus, expected to be  
6 higher when the glass plate is grounded. Indeed, the electric potential of the glass plate is normally zeroed  
7 when it is grounded. On the contrary, it is expected to be higher when the plate is at a floating potential.  
8 Therefore, the electric potential difference between the high-voltage electrode and the plate's surface is  
9 higher in the case of a grounded plate, resulting in a higher axial electric field. This was also concluded in  
10 a recent study [49], which focused, however, on the interaction of a He APPJ with a quartz plate (at a  
11 floating potential or grounded) placed 20 mm away from the tube's orifice. The authors studied the  
12 propagation dynamics and the maximum amplitude of the electric field ( $E_{MAX}$ ) of the guided streamers by  
13 means of ICCD imaging and numerical modeling, respectively. When the plate was grounded, the intensity  
14 of the emission of the guided streamers, and the  $E_{MAX}$  close to the target's surface were clearly higher,  
15 corroborating the results shown in figure 3(a). Furthermore, in our case, besides the difference in the APPJ  
16 emission intensity between the floating-potential and the grounded plate, the corresponding temperatures  
17 of the glass plate differ significantly. Figure 3(b) shows representative IR images for both cases. Indeed,  
18  $T_{Plate}$  increases drastically up to  $\sim 80 \pm 3$  °C when the plate is grounded, while, for a floating-potential plate,  
19 it is always lower than  $30 \pm 3$  °C (see also [4] for detailed studies of the  $T_{Plate}$  in this case). Note that those  
20 temperatures are obtained from single shot measurements, where the error margins of 3 degrees refer to the  
21 accuracy of the measurement given by the camera manufacturer. A detailed statistical analysis of those  
22 temperatures is given in figure 6. The higher  $T_{Plate}$  recorded for a grounded glass plate is attributed to heating  
23 processes (Ohmic effects) caused by the current  $I_{Plate}$ . Furthermore, the higher emission intensity of the  
24 APPJ when impinging on a grounded plate denotes enhanced excitation and ionization processes in the  
25 APPJ channel, possibly due to the higher axial electric field and electron density compared to those  
26 corresponding to a floating-potential plate. The APPJ is also hotter in the case of a grounded plate, and,  
27 therefore, besides ohmic effects, the glass plate is also heated due to the higher temperature of the argon  
28 gas (see figures 6 and 7).  
29  
30  
31  
32  
33  
34  
35  
36  
37  
38  
39  
40  
41  
42  
43  
44  
45  
46  
47  
48  
49  
50  
51  
52  
53  
54  
55  
56  
57  
58  
59  
60

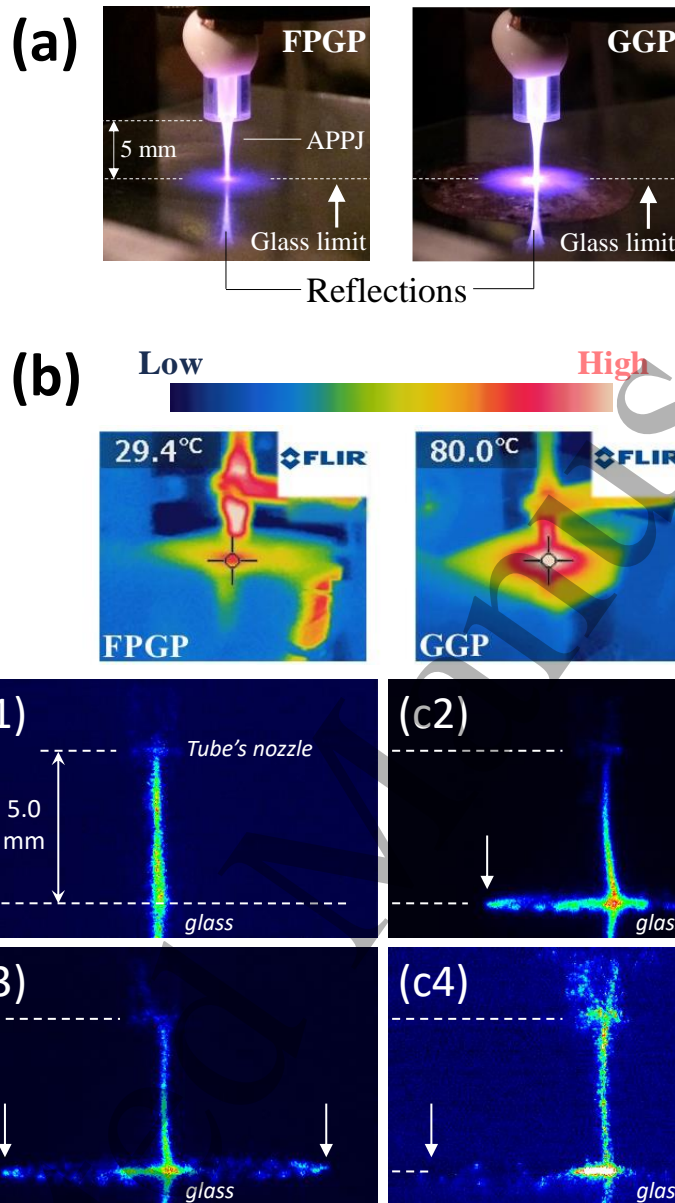
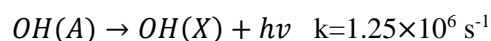


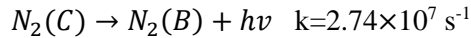
**Figure 3.** (a) High-definition photos of the APPJ (wavelength-integrated emission in the UV-VIS spectral range; exposure time=60 ms) impinging on a floating potential (FPGP, left) and a grounded glass plates (GGP, right). (b) False-color IR camera images used to evaluate the temperature of the glass plate at the impact spot of the APPJ with the floating-potential (left) and the grounded (right) plate. (c) Wavelength-integrated ICCD images of the APPJ and the surface ionization wave (SIW) at the following instants after  $t_0$  (cf. figure 2(b)): (c1)  $t_i$ : when the APPJ strikes on the glass surface, slightly before the inversion of the  $I_{DBD}$ , (c2)  $t_m$ : when  $I_{Plate}$  reaches its peak, (c3) when (after  $t_m$ )  $I_{Plate}$  falls to half of its peak value, and (c4)  $t_e$ : when  $I_{Plate}$  and  $I_{DBD}$  are zeroed. In figures 3(c2)–3(c4), the distance between the white arrows corresponds to the diameter of the area covered by the SIW (luminous “disk” in figure 3(a)): 9, 11 and 13 mm, respectively. All images are recorded using a 3 ns ICCD gate over only one single voltage pulse. The light scale is the same for figures 3(c1)–3(c3), but figure 3(c4) is significantly intensified as compared to the others due to the very weak intensity of the APPJ emission at  $t_e$ .

1  
2  
3 The dynamics of the studied APPJ impinging on a floating-potential plate has been investigated  
4 thoroughly lately by our group using ICCD imaging [27]. As so, using the same technique, the present work  
5 focused only on the dynamics of the APPJ impinging on a grounded plate, which has not been studied yet.  
6 This is of interest herein for the analysis of the propagation dynamics of the surface ionization wave on the  
7 glass plate and its correlation with the temporal evolution of the current  $I_{\text{Plate}}$ .  $I_{\text{Plate}}$  starts to form right after  
8 the strike of the streamer's head on the glass surface (instant  $t_i$  in figure 2(b)). The corresponding ICCD  
9 image of the wavelength-integrated APPJ emission is shown in figure 3(c1). At the contact point, the width  
10 of the streamer head is only  $\sim 0.8$  mm, leaving behind it a rather diffuse conductive plasma channel of a  
11 similar thickness, which extends up to the orifice of the reactor's tube. According to the orientation of the  
12 current probes used, the current is positive when the electrons flow towards the high-voltage electrode. As  
13 so, when the jet hits the plate at  $t_i$ , positive electrical charges start to accumulate on the glass surface. Due  
14 to this positive electrical charge buildup and the continuously decreasing applied voltage after the instant  
15  $t_i$ , more and more electrons start to flow towards the target. This is what is observed in figure 2(b) just after  
16 the instant  $t_i$  when an inversion of the DBD current (black color) is recorded, being maximized (absolute  
17 value) slightly before the instant  $t_m$ . At the same time, the current  $I_{\text{Plate}}$  in figure 2(b) (green) is positive,  
18 which means that electrons in the wire under the glass are also flowing towards the plate, being attracted  
19 by the positive electrical charges deposited on its surface.

20 Furthermore, figure 3(c2) refers to the instant  $t_m$  in figure 2(b), i.e. when the positive peak value of the  $I_{\text{Plate}}$   
21 is reached. One can easily distinguish the bright spot formed at the contact point in agreement with figure  
22 3(a). The diffuse residual channel of the streamers is still visible in figure 3(c2), indicating a highly  
23 conductive APPJ. However, compared to figure 3(c1), it is slightly thinner, and its emission intensity is  
24 much weaker in the axial zone  $0 \leq z < 2$  mm, while for  $z \geq 2$  it is displaced slightly from the axis ( $y=0$ ). It  
25 indicates a less stable APPJ when using a grounded plate, in agreement with the fluctuation observed on  
26 the corresponding absorption and current signals. A remarkable spreading of the surface ionization wave  
27 on the glass surface is revealed, covering an area of 9 mm in diameter (figure 3(c2)) in just 35 ns (i.e.  
28 between  $t_i$  and  $t_m$  in figure 2(b)). The surface ionization wave continues to propagate even after the instant  
29  $t_m$ , attaining a distance of 11 mm when  $I_{\text{Plate}}$  falls to the half of its peak value (see figure 3(c3)). The diffuse  
30 residual channel (mostly in the zone  $z \geq 2.5$  mm), and the bright spot are still distinguishable in figure 3(c3).  
31 This implies that the electric field after the passage of the ionization front is still high enough to sustain  
32 ionization and excitation (see later in the text for identification of various reactive species). Argon  
33 metastables can have an indirect role on the light emission in this case. For instance, these species can be  
34 involved in the generation of  $\text{OH}(A^2\Sigma^+)$  and  $\text{N}_2(\text{C}^3\Pi_u)$ , which later decay radiatively to their ground states  
35 as follows [53,54]:



56  
57  
58  
59  
60



Both transitions are clearly detected in the emission spectrum of the APPJ (see figure 5). A similar spreading phenomenon of the surface ionization wave has been reported in He APPJs impinging on dielectric targets [10,11,48,52]. As explained previously and in agreement with the literature, due to a positive electrical charge accumulation on the dielectric, an axial electric field is formed, which opposes that of the streamer. The radial component of the electric field becomes dominant assisting the development of a surface ionization wave [15]. This was confirmed by another recent numerical study of a He APPJ impinging on a floating dielectric target [45], where the surface ionization wave spread over the target is predicted in agreement with [15]. The maximum propagation distance of the surface ionization wave is, in our case, of 13 mm (figure 3(c4)), and it is 1.25 times higher than that recorded while using a floating-potential glass plate [27] (see also figure 3(a)). It is attained at the instant  $t_e$  in figure 2(b), i.e. when the  $I_{\text{plate}}$  and the  $I_{\text{DBD}}$  are zeroed and the applied voltage has decreased to  $\sim 80\%$  of its peak value. After the instant  $t_e$ , the intensity of the emission originating from the surface ionization wave progressively decreases until its extinction at the end of the applied voltage pulse, due to a compensation of the deposited electrical charges. Note, finally, that the APPJ emission in figure 3(c4) was significantly intensified in order to become visible. In fact, the APPJ intensity in figure 3(c4) is much lower than in figures 3(c1)-3(c3).

Works concerning interactions of Ar APPJs with dielectric targets (grounded or not) are also available in the literature [19-24,55-57]. Most of them, though, use AC waveforms (kHz–MHz frequency range) for plasma generation, and the APPJ characterization is done by means of voltage-current, time-integrated imaging, and emission spectroscopy methods [19-22,56,57]. Only few works, also using AC power supplies, have combined the previous experimental methods with ICCD imaging for similar studies [23,24,55]. The present work uses a kHz ns-pulsed excitation to form an Ar APPJ. The experimental characterization of its interaction with a grounded glass target is achieved by combining, for the first time here, electrical diagnostics, emission spectroscopy, time-resolved ICCD imaging, and, as discussed in the next section, TDLAS for the precise mapping of the absolute radial density of Ar( $1s_5$ ) metastables (see figures 2–5).

## 2. Space-time resolved Ar( $1s_5$ ) density and APPJ spectroscopic analysis

Figure 4(a1) depicts the temporal evolution of the line-of-sight averaged density of Ar( $1s_5$ ) for a floating-potential glass plate (black), measured at  $z=4.8$  mm and  $y=0$ . This is the position of most interest regarding the desired application of this work. In this case, the Ar( $1s_5$ ) average density exhibits two temporal peaks ( $P_{1F}$  and  $P_{2F}$ ). It reaches fast its maximum value ( $P_{1F} \approx 9 \times 10^{12} \text{ cm}^{-3}$ ), followed shortly ( $\sim 40$  ns later) by a second slightly smaller peak ( $P_{2F} \approx 8.5 \times 10^{12} \text{ cm}^{-3}$ ), and, then, it is zeroed in less than 600 ns. A rather similar tendency is observed for the temporal variation of the total plasma emission recorded by the photodiode

(shown in red in figure 4(a1)), which, however, refers to the UV–NIR spectral region and decreases relatively faster. The leading edge of the Ar(1s<sub>5</sub>) line-of-sight averaged density signal (see instant t<sub>1F</sub> in figure 4(a2)) coincides with that of the total plasma emission originating from the streamer's head (compare black and red curves in figure 4(a1)). As so, P<sub>1F</sub> refers to the production of Ar(1s<sub>5</sub>) in the streamer's head by direct impacts with energetic electrons generated by the passage of the streamer [4,27]. After the peak P<sub>1F</sub>, the density decreases sharply in about 20 ns up to the instant t<sub>2F</sub>. This decrease is attributed to the loss of Ar(1s<sub>5</sub>) through their excitation to higher energy states of argon by collisions with electrons, which are still present in high densities in such short delay [44].

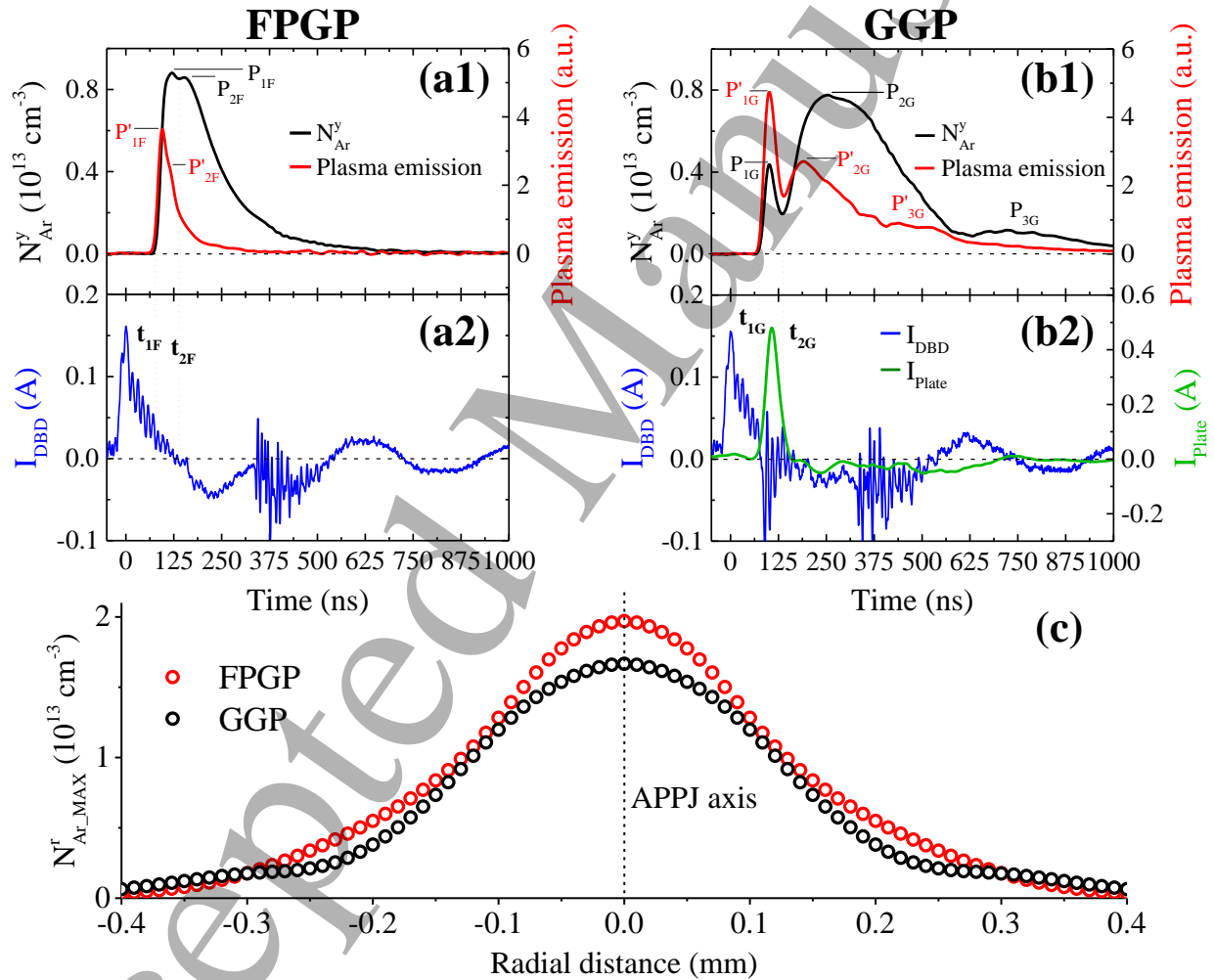


**Figure 4.** Temporal evolution of the line-of-sight averaged density of Ar(1s<sub>5</sub>) ( $N_{Ar}^y$ , black) and the wavelength-integrated (320–1000 nm) plasma emission (red) at  $z=4.8$  mm and  $y=0$ , I<sub>DBD</sub> (blue) and I<sub>Plate</sub> (green) in the case of a floating-potential (FPGP, (a1) and (a2)) and a grounded (GGP, (b1) and (b2)) glass plate. (c) Ar(1s<sub>5</sub>) maximum density symmetric radial profiles ( $N_{Ar\_MAX}^r$ ) at  $z=4.8$  mm. All sub-figures show average waveforms obtained from 1000 signals in the oscilloscope.

$P_{2F}$  is obtained  $\sim 20$  ns later than the instant  $t_{2F}$  in figure 4(a2) (i.e. when the inversion of  $I_{DBD}$  starts). The formation of  $P_{2F}$  in the residual channel of the streamers can be related to the small inflection point of the total plasma emission ( $P'_{2F}$ ) in figure 4(a1). This small inhibition of the decrease of the total plasma emission at  $P'_{2F}$  indicates that, among other emissions, more Ar( $2p_i$ ) states ( $i=2, 3, 6, 8, 9,$  and  $10$ , see below for details) are de-excited through radiative relaxations to the  $1s_5$  level assisting, thus, the formation of metastables at  $P_{2F}$ . For the present argon APPJ, Sousa *et al.* [44] measured the temporal evolution (after the peak of  $I_{DBD}$ ) of the electron density ( $n_e$ ) and temperature ( $T_e$ ) in the case of a floating-potential glass plate placed, as in our case, at 5 mm from the tube's nozzle. At  $z=3.6$  mm, close to the instant of appearance of  $P_{1F}$ ,  $n_e$  was found to be  $\sim 9 \times 10^{13} \text{ cm}^{-3}$ , while close to  $P_{2F}$  (i.e. in the diffuse residual channel behind the streamer's head), it was still relatively high,  $\sim 7.5 \times 10^{13} \text{ cm}^{-3}$ . Between those instants,  $T_e$  was found to be around 1 eV. These values are expected to be higher when the target is grounded [10,11,45]. Anyway, the electron density at  $t_{2F}$  being similar to that at  $t_{1F}$ ,  $P_{2F}$  (as  $P_{1F}$ ) can be the result of Ar( $1s_5$ ) excitations by direct electron impacts. Based on the findings of [40], it is proposed that the largest contributors to the formation of the peak  $P_{2F}$  are electron-impact excitations and deexcitations of upper states through photon emissions or transfers from the other  $3s$  states by collisions with Ar. It should be noted that in the case of a floating-potential plate we did not observe the initiation of a secondary ionization front (no evidence on the signals of the total plasma emission (figure 4) nor on the ICCD imaging (3 ns gate)). In [45], for a helium APPJ impinging on a floating-potential dielectric target, a secondary ionization front was detected, which, however, decayed rapidly by few nanoseconds after the impingement of the primary ionization front on the dielectric target. Therefore, the interaction of APPJs with dielectric targets enables rather the development of a surface ionization wave on the target surface than a secondary ionization front, as it happens with conductive targets [10,11,45].

Some of the mechanisms responsible for the formation of  $P_{2F}$  were discussed in more detail in [27], and this study focuses only on the differences observed in the line-of-sight averaged density of Ar( $1s_5$ ) between using a floating-potential and a grounded glass plate. Interestingly, the line-of-sight averaged density of Ar( $1s_5$ ) exhibits three temporal peaks when using a grounded glass plate ( $P_{1G}$ ,  $P_{2G}$  and  $P_{3G}$  in figure 4(b1)). Similarly to the floating-potential case, the leading edge of the line-of-sight averaged density of Ar( $1s_5$ ) coincides with that of the total plasma emission (see instant  $t_{1G}$  in figure 4(b2)). As so,  $P_{1G}$  ( $\approx 4.3 \times 10^{12} \text{ cm}^{-3}$ ) is linked to  $P'_{1G}$  and, like  $P_{1F}$ , is associated with the production of Ar( $1s_5$ ) metastables in the streamer's head. Furthermore,  $P_{2G}$  ( $\approx 7.7 \times 10^{12} \text{ cm}^{-3}$ ), as  $P_{2F}$ , is due to the production of Ar( $1s_5$ ) metastables in the diffuse channel left by the guided streamers [27,38], and it is also related to the second peak of the total plasma emission ( $P'_{2G}$  in figure 4(b1)).  $P'_{1G}$  and  $P'_{2G}$  exhibit, however, higher amplitudes as compared to  $P'_{1F}$  and  $P'_{2F}$ , and their formation starts at the instants  $t_{1G}$  (i.e. when  $I_{DBD}$  is inversed) and  $t_{2G}$  (i.e. when the positive  $I_{plate}$  and the negative  $I_{DBD}$  are practically zeroed), respectively. Note that such

1  
2  
3 inversion of the DBD current is not observed between  $t_{1F}$  and  $t_{2F}$  when using a floating-potential glass plate  
4 because the glass plate is not grounded. This current inversion is due to an inversion of the direction of  
5 propagation of electrons in the APPJ, which could possibly lead to the higher amplitudes of the first two  
6 peaks of the total plasma emission when using a grounded glass plate. After the instant  $t_{2G}$ ,  $I_{\text{plate}}$  (for the  
7 first time) and  $I_{\text{DBD}}$  (for the second time) become negative and they seem to be minimized at the same  
8 instant, coinciding also with that of the maximum of the line-of-sight averaged density of  $\text{Ar}(1s_5)$  ( $P_{2G}$ ,  
9 around 250 ns in figure 4(b2)).  $P_{2G}$  is obtained quite later than  $P_{2F}$ , and it is 44% higher than  $P_{1G}$ . For a  
10 floating-potential glass plate, however,  $P_{2F}$  is 5% lower than  $P_{1F}$ . Assuming that the  $\text{Ar}(1s_5)$  losses are the  
11 same between the floating-potential and grounded plate conditions, this fact denotes that the production of  
12  $\text{Ar}(1s_5)$  in the residual channel of the streamers is higher in the case of a grounded glass plate. This is  
13 because the production mechanisms of the  $\text{Ar}(1s_5)$  metastables are more effective when using a grounded  
14 plate (e.g. enhanced excitation through electron impacts). On the other hand,  $P_{2G}$  is slightly lower than  $P_{1F}$   
15 and the corresponding maximum radial density of metastables (figure 4(c)) is also slightly lower as  
16 compared to a floating-potential plate. Indeed, a maximal radial density of up to  $\sim 2 \times 10^{13} \text{ cm}^{-3}$  is obtained  
17 on the APPJ axis at  $z=4.8$  mm for a floating-potential plate (figure 4(c)), which is  $\sim 17\%$  higher than that  
18 obtained when using a grounded plate. However, as the signal fluctuation increases by 33% when using a  
19 grounded plate instead of a floating-potential plate (for detailed results on the absorbance signal fluctuations  
20 in the case of a floating-potential plate see [27]), the maximum radial density values are, in fact, quite  
21 similar in both cases. The measurement of the  $\text{Ar}(1s_5)$  absolute radial density in a ns-pulsed Ar APPJ  
22 impinging on a grounded dielectric target is achieved, for the first time, in this work. In fact, the absorption  
23 signal is reasonably reproducible along the y axis to perform a reliable measurement of the  $\text{Ar}(1s_5)$  absolute  
24 radial density. This was checked by carrying out several transversal mappings of the average maximum  
25 absorption at  $z=4.8$  mm (not shown). The average value and the standard deviation were deduced from  
26 1000 single-shot absorption signals recorded in the oscilloscope. In figure 4(c), the small difference on the  
27 average maximum radial densities of  $\text{Ar}(1s_5)$  between the two electric potential conditions was preserved  
28 within the radial ( $r$ ) zone  $-0.05 < r < 0.05$  mm. For  $r < -0.05$  and  $r > 0.05$  mm, the densities were lower and quite  
29 close in both cases. For a floating-potential plate, the maximum radial density of  $\text{Ar}(1s_5)$  decreased radially  
30 reaching its zero value at  $r \approx \pm 0.35$  mm. For a grounded plate, though, a slightly higher density was found at  
31 the wings of the radial profile ( $-0.4 < r < -0.25$  and  $0.25 < r < 0.4$  mm), leading to a little larger radial expansion,  
32 in good agreement with that of the wavelength-integrated emission of the APPJ (see figure 3(a) and figure  
33 3(c4)). The decrease of the maximum radial density at high radial coordinates in both cases should be  
34 attributed to the quenching of  $\text{Ar}(1s_5)$  by air species, which diffuse into the argon gas jet gradually more  
35 and more with increasing radial distance, and to the decrease of the electron density and/or the radial electric  
36 field amplitude when moving from the axis to the edges of the APPJ [27,44,53,58].  
37  
38  
39  
40  
41  
42  
43  
44  
45  
46  
47  
48  
49  
50  
51  
52  
53  
54  
55  
56  
57  
58  
59  
60

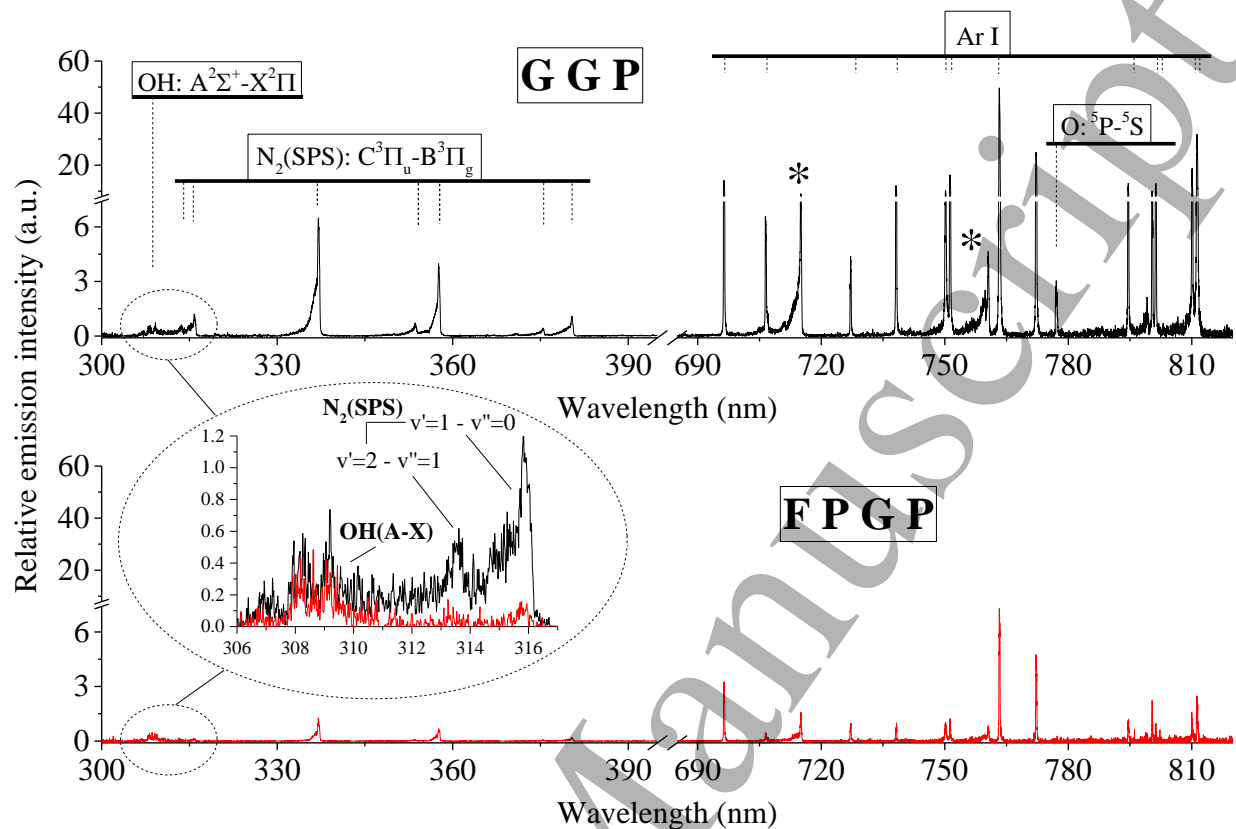


**Figure 5.** Emission spectrum (UV–NIR) of the APPJ in the case of a grounded (GGP, black, upper frame) and a floating-potential (FPGP, red, lower frame) glass plate. The inset is a zoom in the spectral region 306–316 nm. The asterisks denote second-order spectra of the  $N_2(\text{SPS})$ .

Another interesting result is illustrated in figure 4(b1). When the plate is grounded,  $\text{Ar}(1s_5)$  metastables are maintained for much longer time in the diffuse channel left by the streamers (possibly due to an enhancement of the axial electric field and electron density as compared to those when the plate is at a floating-potential), promoting in this way further energy transfer reactions such as the excitation of  $N_2(X)$  to the  $N_2(C)$  level. The latter process was studied in more detail in a freely expanding  $\mu\text{s}$ -pulsed He/Ar APPJ [38]. The temporal evolution of the line-of-sight averaged density of  $\text{Ar}(1s_5)$  and the  $N_2(C-B)$  emission intensity in the residual streamer channel were compared. The obtained results revealed an extended afterglow emission from the  $N_2(C-B)$ , which was primarily maintained by energy transfer from  $\text{Ar}(1s_5)$  metastables. This is in good agreement with the results of figure 4. Indeed, the temporal evolution of the line-of-sight averaged density of  $\text{Ar}(1s_5)$  (black) and the total plasma emission (red) correlate quite well, confirming the results obtained in [38]. Even if the emission of  $N_2(C-B)$  cannot be extracted from the plasma emission signals of figures 4(a1) and 4(b1), this species is assumed to have a significant contribution to the total plasma emission (see figure 5). Therefore, the energy transfer reaction proposed in [38] is

1  
2  
3 expected to be very effective under our experimental conditions. Besides, its significance has been  
4 demonstrated in a recent study of our group [27], and it is further discussed later.  
5

6 The observed differences on the spatio-temporal absolute density of Ar( $1s_5$ ) between using a  
7 floating-potential and a grounded glass plate suggest a role of the current  $I_{\text{plate}}$  (figure 2(b) and figure 4(b2)).  
8 As it was discussed in the description and analysis of figures 2 and 3, the production/loss mechanisms of  
9 Ar( $1s_5$ ) as well as of other reactive species should be affected by the presence of  $I_{\text{plate}}$ . The production of  
10 Ar( $1s_5$ ) can be done through i) electron impact excitation, ii) radiative relaxation of higher energy 2p levels  
11 to the  $1s_5$  level, and iii) radiative recombination of electrons with argon ions. The quenching of Ar( $1s_5$ ) is  
12 due to three-body collisions with ground-state Ar and energy transfer reactions with air species [27,38].  
13 Some of these mechanisms can be studied in more detail by analyzing the effect of the electric potential of  
14 the glass plate on the wavelength-resolved emission of the APPJ. This was achieved in this work by means  
15 of optical emission spectroscopy. The corresponding spectra are shown in figure 5; they refer to the space-  
16 time integrated plasma emission recorded throughout the 5 mm-gap using the same slit width and  
17 integration time. At a glance, numerous transitions of radiative species are revealed, namely OH(A-X),  
18 N<sub>2</sub>(SPS), excited argon and atomic oxygen (see characteristic molecular bands and atomic lines in figure  
19 5). It is remarkable that the peak intensity of all argon lines is significantly higher when using a grounded  
20 plate. Depending on the atomic line, an increase between 77% ( $2p_2-1s_5$  at 696.5 nm) and 93% ( $2p_9-1s_5$  at  
21 811.5 nm) was measured. This fact signifies enhanced excitations of Ar atoms through electron impacts,  
22 validating the hypothesis of a more conductive APPJ channel when the glass plate is grounded.  
23 Furthermore, in the spectral region 690-840 nm, about 43% of the detected excited argon species contribute  
24 to the production of Ar( $1s_5$ ). They refer to the radiative transitions  $2p_2-1s_5$ ,  $2p_3-1s_5$ ,  $2p_6-1s_5$ ,  $2p_8-1s_5$ ,  $2p_9-$   
25  $1s_5$  and  $2p_{10}-1s_5$ . Therefore, compared to the use of a floating-potential plate, a significant increase of the  
26 density of Ar( $1s_5$ ) should be expected in the case of using a grounded plate. This is seen in figure 4(b1), as  
27 the line-of-sight averaged density of Ar( $1s_5$ ) is noticeably higher for a grounded plate in the range 250-1000  
28 ns (i.e. slightly before, and after the peak  $P_{2G}$ ).  
29

30 Note also the formation of a third small peak on the total plasma emission ( $P'_{3G}$  in figure 4(b1)),  
31 which is observed only when using a grounded plate, and could assist further the Ar( $1s_5$ ) production. The  
32 Ar( $1s_5$ ) line-of-sight averaged density reaches a minimum ( $\sim 0.9 \times 10^{12} \text{ cm}^{-3}$ ) at about 625 ns, which is  
33 followed by a third peak ( $P_{3G} \approx 10^{12} \text{ cm}^{-3}$ ). After being inversed at  $\sim 550$  ns,  $I_{\text{DBD}}$  reaches a local maximum  
34 of 0.05 A at 625 ns, and the  $I_{\text{plate}}$ , while still being negative, increases towards zero. As a result, an increment  
35 of the Ar( $1s_5$ ) line-of-sight averaged density is initiated up to the peak  $P_{3G}$ , which is reached when both  
36 currents are zeroed (around 750 ns in figure 4(b2)). Then, the line-of-sight averaged density of Ar( $1s_5$ )  
37 decreases continuously, and it is zeroed in less than 500 ns. It should be noted that a similar inversion of  
38 the  $I_{\text{DBD}}$  is recorded with a floating-potential plate (see figure 4(a2)), however, the third temporal peak of  
39  
40  
41  
42  
43  
44  
45  
46  
47  
48  
49  
50  
51  
52  
53  
54  
55  
56  
57  
58  
59  
60

1  
2  
3 the averaged density is not seen in this case. This could be related to the lower amplitude of the axial electric  
4 field and the lower electron density after the passage of the ionization front when using a floating-potential  
5 plate, and it is further discussed below. The formation of a third peak of the Ar( $1s_5$ ) line-of-sight averaged  
6 density was also reported in a previous work of our group studying the same Ar APPJ [40]. However, the  
7 Ar flow rates used therein were from 2.5 up to 3.33 times higher (from 0.75 to 1 l/min, instead of 0.3 l/min  
8 in this work), and the APPJ was not in contact with a target. The appearance of this peak was attributed to  
9 the focus of energetic electrons towards the jet axis that is caused by the accumulation in the jet-air boundary  
10 of negative ions between consecutive voltage pulses. This process occurs at pulse repetition frequencies  
11 higher than 5 kHz [59]. Negative ions are created by dissociative attachment of ambient air species ( $O_2$ ,  
12  $H_2O$ ) during the passage of the ionization front. In the periphery of the APPJ, the passage of the ionization  
13 wave produces additional electrons by detachment processes from those electronegative species. The  
14 intense radial electric field [18,58] induces an acceleration of these electrons towards the center of the jet,  
15 and a subsequent production of Ar( $1s_5$ ) by electron impact. The change in the direction of propagation of  
16 these electrons induces a variation in the DBD and APPJ current. In this work, a third peak on the Ar( $1s_5$ )  
17 line-of-sight-averaged density is not observed when using a floating-potential plate (figure 4(a1)). In fact,  
18 the presence of this peak depends on the gas flow rate ( $Q$ ) and the electric potential of the target. For the  
19 target-free APPJ, it is absent for  $Q < 0.6$  l/min and it becomes apparent only for  $Q > 0.6$  l/min. This is also  
20 true when the APPJ impinges on a floating-potential plate. However, when a grounded plate is used, the  
21 third peak is observed even at a much lower gas flow rate of 0.3 l/min. As discussed before,  $I_{\text{plate}}$  should  
22 play a role in the temporal production of Ar( $1s_5$ ) in this case. Nevertheless, more detailed studies on the  
23 influence of those parameters on the formation of the third peak of the Ar( $1s_5$ ) line-of-sight-averaged  
24 density are necessary to better understand this behavior. A similar stepwise production of He metastables  
25 was recently reported for a He APPJ impinging, however, on a grounded metallic target [9]. It was well-  
26 correlated with a restrike of the ionization wave after its impact on the conductive target. In the present  
27 work, the Ar APPJ impinges on a dielectric target, which rather enables the development of a surface  
28 ionization wave on the target [15,45]. As suggested in [45], in the case of a floating potential plate, a weak  
29 counter propagating ionization wave can be formed, which, however, decays rapidly by few nanoseconds  
30 after the impingement of the primary ionization wave on the target. Low-permittivity materials (as the one  
31 used in this work) are expected to be fully charged at the end of the applied voltage pulse. At this instant,  
32 the voltage is removed from the gap and the electric field is low [11]. Herein, this is well observed when  
33 using a floating-potential plate, since the Ar( $1s_5$ ) line-of-sight-averaged density is zeroed at the end of the  
34 applied voltage pulse (around 1000 ns in figure 4(a1)). For a grounded plate, however, it seems that the  
35 electric field and/or the electron density in the residual channel are relatively higher compared to those of  
36 a floating-potential plate, leading to a more effective excitation of ground-state Ar to the Ar( $1s_5$ ) metastable  
37  
38  
39  
40  
41  
42  
43  
44  
45  
46  
47  
48  
49  
50  
51  
52  
53  
54  
55  
56  
57  
58  
59  
60

1  
2  
3 level. This could also explain the formation of a new peak of the Ar( $1s_5$ ) line-of-sight-averaged density  
4 ( $P_{3G}$ ) around 750 ns in figure 4(b1)).

5  
6 Similarly to the Ar lines, all  $N_2$ (SPS) emissions increase significantly in the case of a grounded  
7 glass plate (80-83% higher intensity is measured for the depicted bands in figure 5). As it was mentioned  
8 before, the loss of Ar( $1s_5$ ) metastables can also be related to the production of  $N_2$ (C) (energy transfer  
9 reaction:  $Ar(1s_5) + N_2(X) \rightarrow N_2(C) + Ar$ ) [23,27,38]. Various  $N_2$ (SPS) transitions are recorded in figure 5  
10 due to the radiative relaxation of  $N_2$ (C) to  $N_2$ (B). Therefore, a fair amount of the total plasma emission is  
11 due to various radiative transitions of the  $N_2$ (SPS) in the APPJ, especially when using a grounded plate.  
12 Besides electronic excitations, the much higher intensity of the  $N_2$ (SPS) in the case of a grounded plate  
13 indicates also a quenching of the Ar( $1s_5$ ) in the excitation process of the  $N_2$ (C) through the above-mentioned  
14 energy transfer reaction [23,27,38]. As a result, the temporal variation of the Ar( $1s_5$ ) line-of-sight-averaged  
15 density should match that of the  $N_2$ (SPS) emission, as in [38]. In our case, the temporal variation of the  
16 total plasma emission matched quite well that of the Ar( $1s_5$ ) line-of-sight averaged density (see figure 4),  
17 in good agreement with reference [38]. Therefore, among the collisional processes leading to the loss of  
18 Ar( $1s_5$ ), energy transfer reactions can play a role when using a grounded plate. The results of figure 5,  
19 showing a higher plasma emission when the plate is grounded, could indicate a higher conductivity of the  
20 APPJ in that case, and are consistent with those reported in [23] (i.e. study of an Ar jet array impinging on  
21 different targets at floating potential and grounded). In that study, it was found that when the jet array  
22 impinged on a grounded metal instead of at a floating potential, the emission intensities of excited Ar and  
23  $N_2$  increased by 74% and 95%, respectively, which corroborates the results of figure 5. They attributed this  
24 difference to the creation of a more conductive discharge channel due to the establishment of a higher axial  
25 electric field. They also suggested a role of the Ar metastables in the excitation of  $N_2$ (C) without, however,  
26 measuring their absolute density. This situation is very similar to our case, even if here a dielectric target is  
27 used instead of a metallic one. Energy transfer processes between Ar( $1s_5$ ) and  $H_2O$  (i.e.  $H_2O + Ar(4p)/Ar(4s)$   
28  $\rightarrow OH(A) + H + Ar$ ) could also lead to the production of OH(A) [53,54], which is detected in figure 5 for  
29 both cases. But a small increase is observed in the OH(A-X) emission when using a grounded plate as  
30 compared to a floating-potential plate (see inset in figure 5). This indicates a rather minor contribution of  
31 the latter reaction to the quenching of Ar( $1s_5$ ) and the production of OH(A) when using a grounded instead  
32 of a floating-potential plate.  
33  
34  
35  
36  
37  
38  
39  
40  
41  
42  
43  
44  
45  
46  
47  
48

49 In the lower spectrum of figure 5 (floating-potential plate), the emission intensity of the atomic  
50 oxygen line at 777.53 nm ( $^5P-^5S$  transition) is comparable to the background noise. On the contrary, this  
51 line is clearly developed in the case of a grounded plate (upper spectrum). This result indicates a much  
52 more efficient dissociation of  $O_2$  (present in the ambient air) through collisions with electrons, excited  $N_2$   
53 and excited Ar [11,39,53] when the glass plate is grounded. This is another evidence that the conductivity  
54  
55  
56  
57  
58  
59  
60

1  
2  
3 of the APPJ and the electric field amplitude increase when using a grounded plate. The mean electron  
4 temperature ( $T_e$ ) and the electron density ( $n_e$ ) in this case are expected to be higher. This hypothesis is  
5 reinforced by the results presented in [50], where an argon APPJ impinging on different metallic objects  
6 (placed at  $z=10$  mm) either grounded or maintained at a floating potential was studied. The current (peak  
7 and time-averaged) and the excitation temperature of the APPJ in the case of the grounded objects were  
8  $\sim 2.5$  and  $\sim 1.14$  times higher, respectively, implying a higher electron density and temperature compared to  
9 those corresponding to the floating-potential objects. This statement is further supported by the results  
10 reported in [45], where the interaction of a ns-pulsed He APPJ with dielectric and metallic targets (grounded  
11 or not) was investigated both experimentally and numerically. Indeed, the simulated electron impact  
12 ionization source and electron density, as well as the simulated velocity and electric field of the ionization  
13 wave were higher for the grounded metal target. Their findings support the results shown in figure 5 and  
14 are in agreement with the higher propagation velocity measured in our case for the grounded plate.  
15 Therefore, we expect a higher electric field, electron density and conductivity in the APPJ when the glass  
16 plate is grounded. For the present APPJ,  $T_e$  and  $n_e$  were evaluated in the past by our group for the case of a  
17 floating-potential glass plate placed, as in the present work, at 5 mm from the tube's nozzle [44]. At  $z=3.6$   
18 mm, values up to 2 eV and  $9 \times 10^{13} \text{ cm}^{-3}$  were reached, respectively (measured 100 ns and 125 ns after the  
19 instant  $t_0$  in figure 2, respectively). Unfortunately,  $T_e$  and  $n_e$  values were not measured for the APPJ in  
20 contact with a grounded glass target due to the unavailability of the laser needed for those measurements.  
21 Nevertheless,  $T_e$  and  $n_e$  are expected to be higher when the plate is grounded [10,45]. In this work, the  
22 vibrational temperature ( $T_v$ ) of the  $N_2(\text{SPS})$  (vibrational sequence  $\Delta v = -2, 365 - 380$  nm) was evaluated  
23 through the Boltzmann-plot method as described in [60]. In agreement with the trends expected for  $T_e$  and  
24  $n_e$ ,  $T_v$  was found to be  $2650 \pm 300$  K and  $2200 \pm 300$  K in the case of a grounded and a floating-potential plate,  
25 respectively. However, taking into account the uncertainties in the  $T_v$  values, the observed difference in  $T_v$   
26 is not significant, and should only be considered a trend. It should also be noted that the concentration of  
27 ozone ( $O_3$ ) is higher when using a grounded glass plate. It was noticed empirically from the smell of its  
28 characteristic odor in the near environment of the APPJ, which was much stronger for a grounded plate.  $O_3$   
29 can be produced through the three-body reaction  $O + O_2 + M \rightarrow O_3 + M$  ( $M$  being a random reaction partner)  
30 [39]. The above results are also in good agreement with simulations reported on a He APPJ impinging on  
31 different targets (from dielectrics to metals) [11]. The authors found that  $n_e$ ,  $T_e$  and the reactive species  
32 concentrations ( $He^*$ , O, OH,  $N_2^*$ ) increase noticeably when the residual channel of the streamers becomes  
33 more conductive (this was achieved by increasing the relative permittivity of a target).  
34  
35  
36  
37  
38  
39  
40  
41  
42  
43  
44  
45  
46  
47  
48  
49  
50  
51  
52  
53  
54  
55  
56  
57  
58  
59  
60

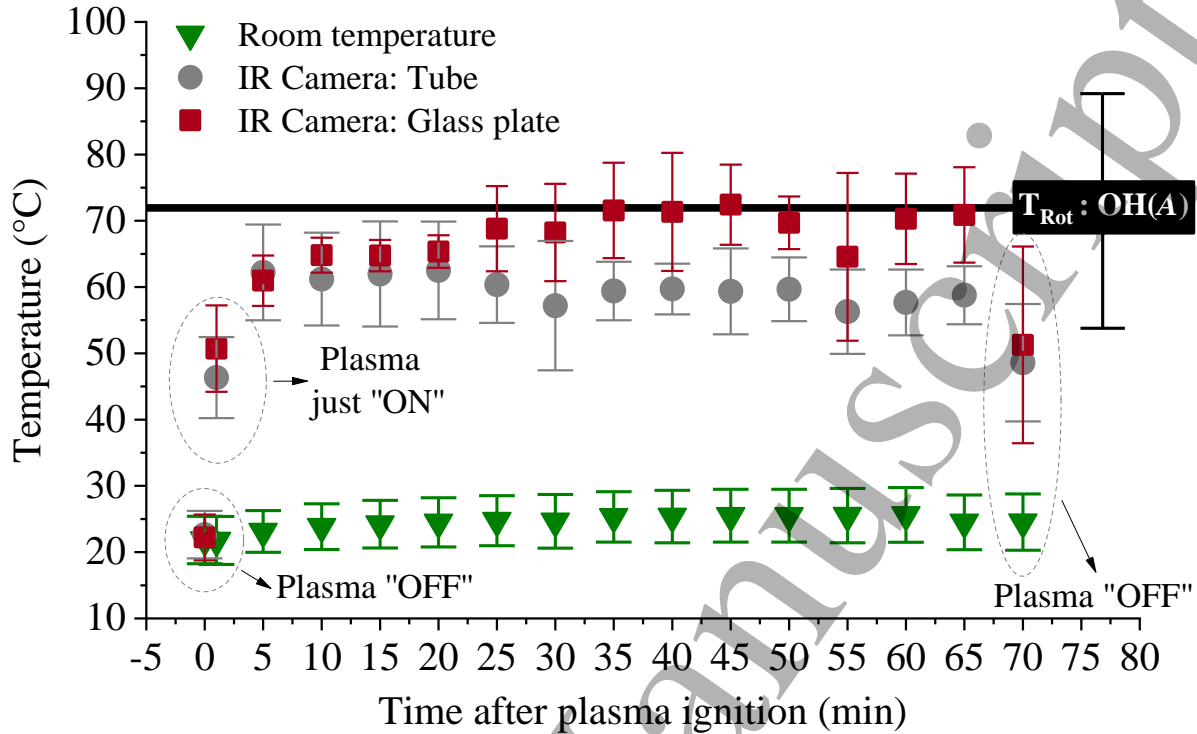


**Figure 6.** Temporal evolution, after the ignition of the plasma, of the temperatures of the capillary tube ( $T_{Quartz}$ ; grey circles) and the glass plate ( $T_{Plate}$ , red squares) in the case of a grounded plate. The green triangles refer to the room temperature ( $T_{Room}$ ). The thick black line refers to the average value of  $T_{Rot}$  of OH(A) (the black caps indicate the standard deviation). Values of  $T_{Room}$ ,  $T_{Quartz}$  and  $T_{Plate}$  refer to four series, while  $T_{Rot}$  refers to three series of experiments performed in different dates. In each series,  $T_{Rot}$  was measured frequently during plasma operation (similarly to  $T_{Room}$ ,  $T_{Quartz}$  and  $T_{Plate}$ ).

Regarding the anticipated application of this work, thermal effects can be significant when using a grounded plate since the temperature of the glass plate can rise up to  $\sim 80 \pm 3$  °C according to the IR image of the right frame of figure 3(b) (single shot value). Figure 6 depicts the temporal evolution, during plasma operation over 70 minutes and in the case of a grounded glass plate, of the following temperatures:  $T_{Room}$  (ambient),  $T_{Quartz}$  (APPJ's tube),  $T_{Plate}$  (glass target) and  $T_{Rot}$  (rotational temperature of OH(A), measured within an APPJ volume corresponding to an axial zone of 2 mm centered at  $z=2.5$  mm; approximately equal to the gas temperature in our case  $\approx T_{Gas}$ ) [20,54]). The corresponding results for the floating-potential plate were presented in [4]. Besides  $T_{Room}$ , which was taken directly from the digital thermometer's indication, the other temperatures were obtained from IR images ( $T_{Quartz}$  and  $T_{Plate}$ ) and from the fitting of high-resolution rotational spectra of OH(A–X) ( $T_{Rot} \approx T_{Gas}$ , see figure 7). In figure 6, the average  $T_{Room}$  increases from 24 °C (when the plasma is “OFF”) to 29 °C (when the plasma has been “ON” for 70 min). When the plasma is “OFF”, the measured  $T_{Room}$  is in very good agreement with  $T_{Quartz}$  and  $T_{Plate}$  (see also the left

1  
2  
3 column of the upper frame of figure 7 – single shot values), validating the measurements performed with  
4 the IR camera. When the plasma is turned “ON”,  $T_{\text{Quartz}}$  and  $T_{\text{Plate}}$  start to rise and, after 5 minutes, they  
5 reach steady-state values of  $56 \pm 10$  °C and  $63 \pm 13$  °C (average values  $\pm$  standard deviations deduced from  
6 all the corresponding averaged  $T_{\text{Quartz}}$  and  $T_{\text{Plate}}$  values shown in figure 6), respectively. Considering the  
7 error bars of the measurements, these values are quite close to  $T_{\text{Gas}}$  of the APPJ which is found to be  $72 \pm 20$   
8 °C (thick black line in figure 6). The evaluation method of the  $T_{\text{Gas}}$  is presented in figure 7. In the case of a  
9 floating-potential plate, thermal desorption effects can be excluded, as  $T_{\text{Plate}}$  and  $T_{\text{Gas}}$  are lower than 30 °C  
10 [4], highlighting the role of Ar( $1s_5$ ) metastables, as the density of oxidative species and ions is also expected  
11 to be lower.

12  
13  
14  
15  
16  
17  
18 The values of  $T_{\text{Plate}}$  and  $T_{\text{Quartz}}$  presented in figure 6 were obtained using various IR images such as  
19 those illustrated in the upper frame of figure 7 (single shots). These offer a better comparison between the  
20 floating-potential and grounded plate conditions. The two images of the left column of the upper frame of  
21 figure 7 give essentially the temperature of the working place (ambient temperature) since, when the plasma  
22 is “OFF”, they agree very well with the first  $T_{\text{Room}}$  value of figure 6 (green triangles). The middle and right  
23 columns are indicative of the differences observed on  $T_{\text{Plate}}$  and  $T_{\text{Quartz}}$  between using a grounded (middle)  
24 and a floating-potential (right) glass plate. The middle column (grounded plate) illustrates two indicative  
25 IR images used for the plotting of  $T_{\text{Plate}}$  and  $T_{\text{Quartz}}$  in figure 6. Comparing them with those of the right  
26 column (floating-potential plate), the impact spot of the APPJ and the circular area covered by the surface  
27 ionization wave are much brighter (similar to figure 3(a)). Moreover, the corresponding  $T_{\text{Quartz}}$  and  $T_{\text{Plate}}$  are  
28  $\sim 2$  and  $\sim 2.9$  times higher, respectively, supporting the hypothesis of non-negligible thermal effects on  
29 bibenzyl desorption when using a grounded plate. The lower frame of figure 7 refers to the case of a  
30 grounded plate. It illustrates a representative synthetic spectrum (red) resulting from the fitting method of  
31 an experimental rotational spectrum of OH(A–X) (black, measured within an APPJ volume corresponding  
32 to an axial zone of 2 mm centered at  $z=2.5$  mm). As it was shown in figure 5, the emission of OH(A) is  
33 present in the emission spectrum of the APPJ. The fitting of its high-resolution rotational spectrum with a  
34 synthetic spectrum has been shown to be a reliable method for the estimation of  $T_{\text{Gas}}$  in pulsed argon APPJs  
35 [54,60], and, thus, it was used here to infer  $T_{\text{Gas}}$  (see figure 6). Results for the case of a floating-potential  
36 plate were presented in [4,27]. The coefficient  $R^2$  of the fitting is also shown in the lower image, attesting  
37 a rather good agreement between the experimental and the synthetic OH(A–X) spectra, in accordance with  
38 similar works [54,60,61].  
39  
40  
41  
42  
43  
44  
45  
46  
47  
48  
49  
50  
51  
52  
53  
54  
55  
56  
57  
58  
59  
60

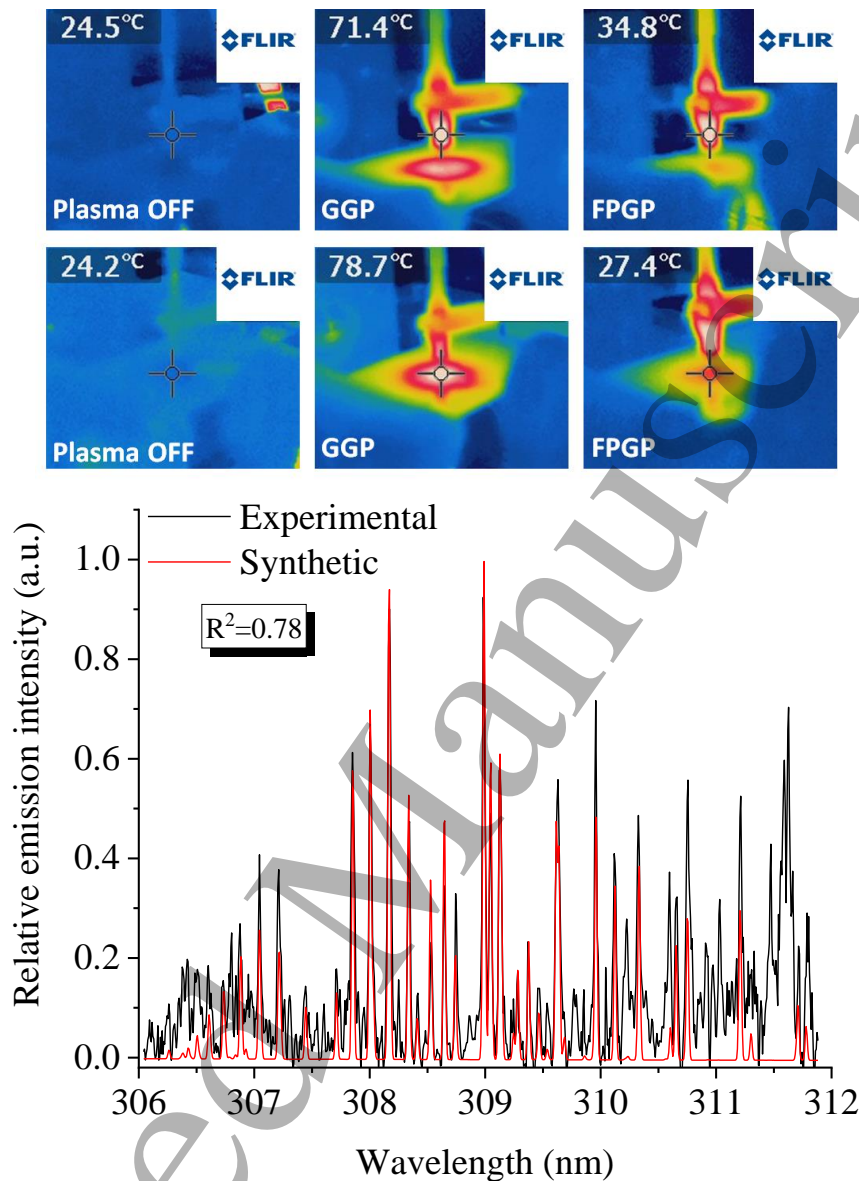


**Figure 7.** Upper frame: false-color IR camera images used to evaluate  $T_{\text{Quartz}}$  (upper images) and  $T_{\text{Plate}}$  (lower images), when using a floating-potential (FPGP, right column) and a grounded (GGP, middle column) glass plate. Images on the left column refer to the case where the plasma was “OFF”. Lower frame: comparison between an experimental (black) and a synthetic (red) rotational spectra of the OH(A–X) used for the evaluation of  $T_{\text{Rot}}$  of OH(A), when using a grounded glass plate.

Note that when the glass plate is grounded, the emission intensity of  $\text{N}_2(\text{SPS})$  is much higher than when using a floating-potential plate. Indeed, this is seen in the inset of figure 5 and, in more detail, in figure 7, where different  $\text{N}_2(\text{SPS})$  vibrational transitions are present within the same spectral region as OH(A–X) (310–312 nm). This affects the fitting of the OH(A–X) rotational spectrum, increasing the fitting error. This is why the standard deviation of  $T_{\text{Rot}}$  of OH(A) is relatively high compared to those of the other

temperatures (see figure 6). For the evaluation of  $T_{\text{Gas}}$ , the APPJ light was collected from a plasma volume corresponding to an axial zone of 2 mm, centered in the gas gap between the tube's nozzle and the glass plate (i.e.  $z=2.5$  mm). By translating the center of the emission volume to  $z=1$  mm (i.e. closer to the quartz tube, where the  $\text{N}_2(\text{SPS})$  intensity is lower [27], and, thus, it perturbs less the  $\text{OH}(A-X)$  spectrum), the obtained  $T_{\text{Gas}}$  is  $55\pm 10$  °C, which is in quite good agreement with the  $T_{\text{Quartz}}$  ( $56\pm 10$  °C). The corresponding standard deviation is 2 times lower than that of  $T_{\text{Rot}}$  determined in the previous zone, due to the relatively lower fitting error ( $\sim 1.9$  times lower), resulting from a smaller perturbation of the  $\text{OH}(A-X)$  rotational spectrum by the  $\text{N}_2(\text{SPS})$ . Finally, when the center of the emission volume was translated to  $z=3.5$  mm (i.e. closer to the glass plate, where the emission intensity of the  $\text{N}_2(\text{SPS})$  is higher [27], and, thus, perturbs more the  $\text{OH}(A-X)$  spectrum),  $T_{\text{Gas}}$  was found to be  $150\pm 60$  °C, indicating that the gas is hotter close to the glass surface. However, the corresponding standard deviation of  $T_{\text{Rot}}$  is 3 and 6 times higher than those of  $T_{\text{Rot}}$  determined in the first (centered at  $z=2.5$  mm) and the second emission volumes (centered at  $z=1$  mm), respectively. Again, this is due to the relatively higher fitting error ( $\sim 3.3$  and  $\sim 6.3$  times higher, respectively), resulting from a higher perturbation of the  $\text{OH}(A-X)$  rotational spectrum by the  $\text{N}_2(\text{SPS})$ . Taking all this into account, it is reasonable to assume that the gas temperature in the case of a grounded plate lies in the range  $90\pm 50$  °C (average value  $\pm$  standard deviation deduced from the mean values of  $T_{\text{Gas}}$  in those three emission volumes).  $T_{\text{Gas}}$  when using a grounded plate is, thus,  $\sim 3.4$  times higher than in the case of a floating-potential plate ( $27\pm 3$  °C [4]). Considering the error bars of  $T_{\text{Gas}}$ , this difference of  $T_{\text{Gas}}$  between the two electric potential conditions is in relatively good agreement with the differences observed on  $T_{\text{Plate}}$ . In fact,  $T_{\text{Plate}}$  is  $\sim 2.5$  ( $63\pm 13$  °C, averaged value  $\pm$  standard deviation of all temporal values of figure 6, versus  $\sim 25\pm 3$  °C, with a floating-potential plate [4]) and  $\sim 2.9$  (figure 7, single shot) times higher when using a grounded glass plate. Therefore, gas heating is more significant when using a grounded plate, and thermal desorption of resistant bibenzyl deposits by the APPJ is possible in this case. This is further studied in the next section.

### C. APPJ desorption efficacy

The metastables of Ar have internal energies of 11.5 and 11.7 eV (for  $1s_5$  and  $1s_3$ , respectively), which are sufficient for the selective desorption and/or ionization of organic molecules from different surfaces. A higher density of Ar metastables should lead to a higher desorption efficiency, since a higher number of metastables impact the Bibenzyl deposits. The  $\text{Ar}(1s_5)$  metastable density measured in the present work is higher than that of the free (no target) Ar APPJ [40]. To the best of our knowledge, only one work studied the effect of a target on the  $\text{Ar}(1s_5)$  densities in Ar APPJs [28]. The APPJ was generated using rf power and it impinged on a floating-potential and a grounded target. Line-of-sight averaged densities of  $\sim 4\times 10^{12}$   $\text{cm}^{-3}$  were measured along the whole plasma channel between the reactor and the target. Compared to [28], the

1  
2  
3 maximum radial density of Ar( $1s_5$ ) generated at the vicinity of the glass target with our system (figure 4) is  
4 5 times higher. Therefore, the measured Ar( $1s_5$ ) metastable densities shown in figure 4 might be high  
5 enough for the desorption of resistant weakly volatile organic compounds. This hypothesis is studied in  
6 detail in this section by analyzing high-resolution stereomicroscope images of resistant bibenzyl deposits  
7 before and after plasma treatment (see figure 8). The images on the far-left side of figure 8 depict the control  
8 samples (not treated). In those images, the dashed yellow circles indicate the position of the dielectric tube  
9 during the plasma treatment, being their diameter the same as that of the tube. Note that the effect of the  
10 APPJ on resistant bibenzyl deposits is investigated thoroughly for the first time in the case of a ns-pulsed  
11 Ar APPJ impinging on a grounded and a floating-potential glass plate (see figure 8). When the plate is  
12 grounded (deposits D3 and D4 of figure 8), a relatively high bibenzyl quantity is desorbed in just 10 s of  
13 plasma treatment (2<sup>nd</sup> column), even much higher at 60 s (3<sup>rd</sup> column), while  $t_{\text{exp}}=180$  s is enough for the  
14 almost complete desorption of the resistant bibenzyl deposit (4<sup>th</sup> column). This is consistent with figure 3(a)  
15 and the upper frame of figure 7, where the bright spot is brighter and wider in the case of a grounded plate,  
16 suggesting a more drastic treatment of the deposited molecules. For a floating-potential plate, however, the  
17 APPJ is clearly less effective on removing bibenzyl molecules in respect to a grounded plate. Indeed, only  
18 a small desorption efficacy is revealed in the upper two frames of figure 8 for  $t_{\text{exp}}=60$  s (deposits D1 and  
19 D2, 3<sup>rd</sup> column). Even if the desorption efficacy is relatively higher at  $t_{\text{exp}}=180$  s (4<sup>th</sup> column), a high amount  
20 of the deposited molecules still remains intact when the glass plate is at a floating potential. The desorption  
21 efficacy for a floating-potential plate becomes significant (i.e. close to that revealed for a grounded plate at  
22  $t_{\text{exp}}\geq 60$  s) only for  $t_{\text{exp}}\geq 600$  s (not shown in figure 8, see figure 9 for details). Therefore, a much higher  
23 desorption efficacy is achieved when using a grounded plate, by reducing significantly the exposure time  
24 to the APPJ needed to obtain the same degree of desorption (compare deposits D1 and D2 with D3 and D4  
25 in figure 8). The application of the gas alone, i.e. when the plasma is “OFF”, to thin deposits of bibenzyl  
26 can have a small influence (negligible compared to that of the plasma) on the bibenzyl removal from the  
27 glass plate (especially for treatment times  $\geq 3$  minutes). This should mean that the bibenzyl molecules  
28 present in the first layer above the lamella are adsorbed to the glass surface and, thus, the bonds between  
29 the bibenzyl and the glass are not strong. Those bonds are most probably much weaker than the bonds  
30 formed between the bibenzyl molecules. Indeed, such an effect of the gas alone was not seen in the large  
31 thick deposit of figure 10, meaning that the bibenzyl molecules are strongly bonded between them.  
32 However, the bonds between the bibenzyl molecules and the glass surface can be considered strong enough  
33 for the bibenzyl deposits to remain intact on the lamellae for many days if no treatment is performed. The  
34 present results agree quite well with those obtained with a He APPJ treating *E. coli* bacteria [49]. The  
35 authors found that the killing of the *E. coli* was much more efficient when using a grounded copper sheet  
36 instead of at a floating potential (the plasma action was evident after just 10 s of exposure, similarly to our  
37  
38  
39  
40  
41  
42  
43  
44  
45  
46  
47  
48  
49  
50  
51  
52  
53  
54  
55  
56  
57  
58  
59  
60

results). They attributed this difference to the production of higher densities of oxidative species in the case of the grounded target. In the present study, however, the much higher desorption efficacy in the case of a grounded plate can be due to a combined action of Ar metastables (they remain for much longer time in the residual channel of the guided streamers, see figure 4(b1)), oxidative species (such as atomic oxygen, hydroxyl radicals and ozone, whose production should be higher for a grounded plate, as expected from the spectra shown in figure 5) and ions. Besides, thermal effects cannot be excluded when using a grounded plate, as it was discussed in detail when analyzing figures 6 and 7.

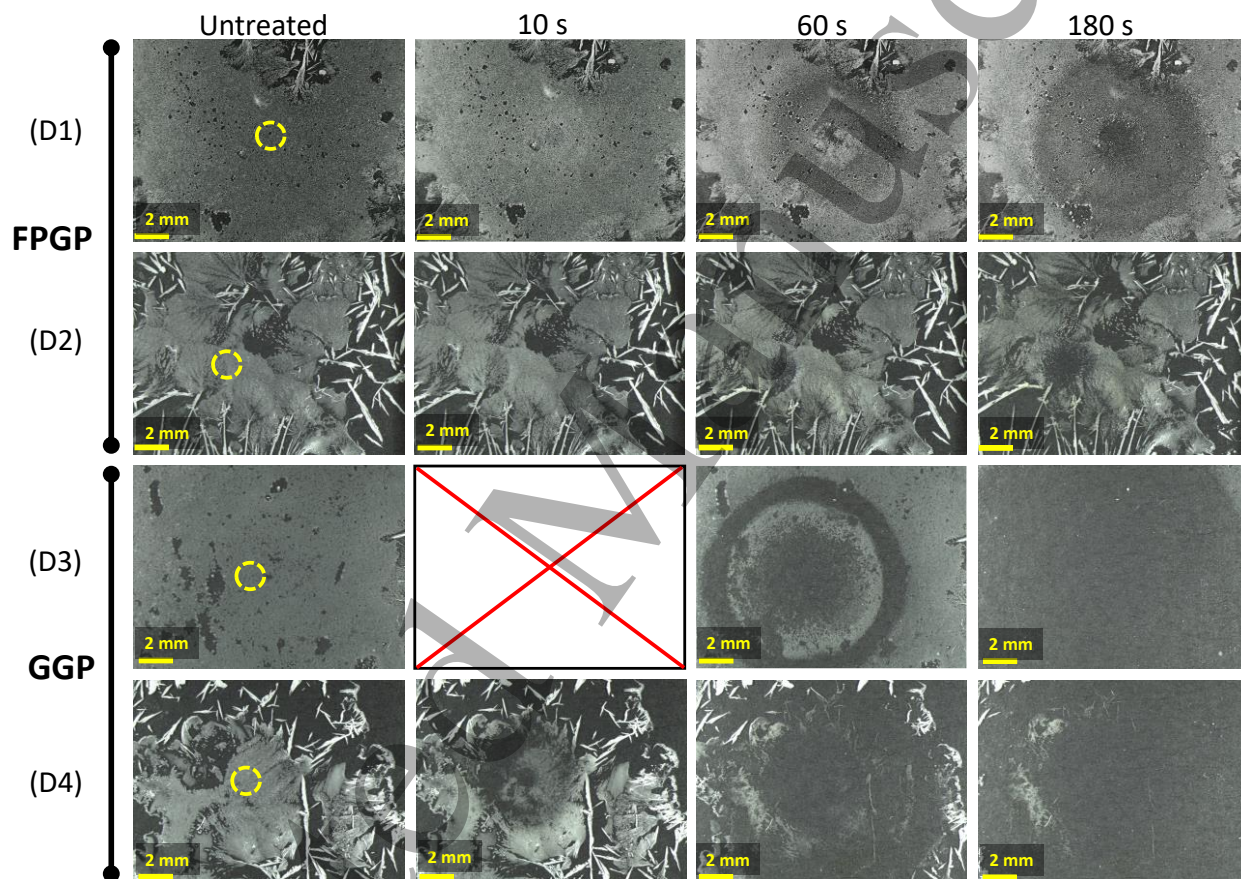


**Figure 8.** D1–D4: high-resolution grey-scale stereomicroscope images of resistant bibenzyl deposits exposed to the Ar APPJ three days after their preparation (exposure times applied: 10 to 180 seconds). D1 and D2 are two different deposits treated in the case of a floating-potential glass plate (FPGP), while D3 and D4 are another two deposits treated in the case of a grounded glass plate (GGP).

More electric power is most probably injected into the APPJ when the plate is grounded, which makes the gas hotter, the APPJ brighter and the production of chemical species higher, as compared to the case of a floating-potential plate (see figures 3-7). This is due to a higher electric current flowing in the reactor-plate direction in the case of a grounded glass plate, which should also contribute further to the removal of bibenzyl molecules from the glass surface. The measurement of the APPJ current is difficult to

perform, preventing a comparison of its contribution to bibenzyl desorption under each electric potential condition of the glass plate. The electric power could be an important factor (if not the most important) behind the better desorption efficacy obtained when using a grounded plate. Decreasing the applied voltage from 6 to 4 kV leads to a reduction of  $E_{\text{DBD}}$  (figure 2(c)) and, thus, to a lower power injected into the APPJ (for both electric potential conditions of the glass plate). As so, the gas and plate temperatures, the APPJ emission intensity (both total and wavelength-resolved), the density of  $\text{Ar}(1s_5)$ , and the current  $I_{\text{Plate}}$  are much lower at 4 kV, due to the corresponding lower injection of electric power. However, for all voltage amplitudes, all the above quantities are clearly larger in the case of a grounded plate, implying enhanced excitations and ionizations in the APPJ volume and, most probably, a more reactive plasma, resulting from a higher electric power injected into the plasma.

A closer inspection of the plasma-treated deposits of figure 8 reveals in some cases the formation of a central spot and concentric rings around it (clearly visible on deposit D1) due to the effect of the APPJ. Such rings and the central spot were also observed in a recent work [55] studying, however, an AC-driven argon APPJ impinging only on a grounded dielectric target. It was found that those rings result from a temporal superposition of filamentary streamers that propagate on the target. To investigate their formation mechanism, the authors combined measurements of the current flowing through the grounded target with fast ICCD imaging. At a peak voltage of 5.1 kV, three concentric luminous rings were formed on the dielectric target. Those are similar with the rings shown in figure 8, which, furthermore, reveals ring formation also when using a floating-potential plate. In [55], the formation of rings was attributed to the generation of distinct streamer discharges (current spikes on the total current signal) in a voltage cycle ( $\sim 15$   $\mu\text{s}$  period). Four discharges ( $D_{\text{ch}_1}$ – $D_{\text{ch}_4}$ ,  $\sim 300$  ns duration) were generated during the positive voltage cycle and only one ( $D_{\text{ch}_n}$ ) during the negative cycle.  $D_{\text{ch}_1}$  and  $D_{\text{ch}_n}$  led to the formation of a bright spot at the contact point of the APPJ with the target.  $D_{\text{ch}_2}$  and  $D_{\text{ch}_3}$ , after covering a certain distance on the target, were split and led to the development of concentric rings. Furthermore, a diffuse background was recorded between those concentric rings due to the propagation of randomly branched streamers from  $D_{\text{ch}_2}$ ,  $D_{\text{ch}_3}$  and  $D_{\text{ch}_4}$ . The behavior of those streamers was qualitatively explained based on the non-uniform distribution of the radial electric field on the target. In figure 8, the density of bibenzyl changes significantly from very low (dark grey zones) to high (light grey zones). Therefore, in our case, enhanced production of reactive species and/or argon metastables should be happening in the dark grey zones (possibly due to a higher reduced electric field amplitude [55]), leading to a more efficient removal of bibenzyl. On the contrary, their density is expected to be lower in the light grey zones due a lower reduced electric field amplitude [55]. A correlation of the ring formation on the grounded glass plate with the spikes on the  $I_{\text{Plate}}$  was not possible in our work. This is attributed to the very different excitation mode between our work and reference [55]. Indeed, a fast voltage pulse ( $\sim 108$  ns rise time, 224 ns FWHM) is used herein to ignite the

1  
2  
3 plasma, instead of the slow AC voltage used in [55] (few  $\mu\text{s}$  rise time,  $\sim 7.5 \mu\text{s}$  half-period). As so, the  
4 energy deposition in the APPJ is much faster and more efficient in our case, and, thus,  $I_{\text{Plate}}$  consists of only  
5 one current pulse (see figures 2 and 4(b2),  $\sim 40 \text{ ns}$  FWHM, which is 6 times faster than the duration of  
6  $D_{\text{ch}_1}$ – $D_{\text{ch}_4}$  in [55]). Therefore, it is assumed that the propagation of the surface ionization wave and the  
7 formation of the rings shown in figure 8 are happening much faster in our case. Nevertheless, a more  
8 detailed study on this phenomenon should be realized under our experimental conditions to better  
9 understand the propagation mechanisms of the surface ionization wave on a floating-potential and a  
10 grounded glass plates. This will be the focus of a future work.

11  
12 The appearance of concentric ring patterns has been also reported in another recent work studying  
13 a  $\mu\text{s}$ -pulsed He APPJ impinging on a floating-potential plate [62]. ICCD images of the total and the filtered  
14 surface ionization wave emission, recorded at  $V_p=8.5 \text{ kV}$  and  $10 \text{ kV}$ , provided a solid evidence of the  
15 formation of annular ring patterns on the dielectric plate resulting from diffuse (at  $8.5 \text{ kV}$ ) and streamer  
16 modes (at  $10 \text{ kV}$ ), in agreement with what was discussed previously. Their results indicate that  $\text{O}(3p^5P)$   
17 and  $\text{N}_2^+(B)$  may be the main contributors to the generation of the diffuse and streamer mode patterns,  
18 respectively. The  $\text{N}_2^+(B)$  mainly focuses on the edge and the center of the spot, whereas  $\text{O}(3p^5P)$  mainly  
19 concentrates on the spot independently of the mode. The differences on the ratio of those two species and  
20 on the local electric field distribution are mainly responsible for the mode transformation observed when  
21 increasing  $V_p$ . In our work, the emission intensity coming from the radiative relaxation of  $\text{O}(3p^5P)$  (figure  
22 5) is negligible when using a floating-potential plate. However, it increases significantly for a grounded  
23 plate, and  $\text{O}(3p^5P)$  could, thus, contribute to the faster removal of bibenzyl from the central spot shown in  
24 figure 8. Indeed, after just  $10 \text{ s}$  of plasma treatment under grounded plate conditions, bibenzyl molecules  
25 have been completely removed from that spot (see figure 8, deposit D4, 2<sup>nd</sup> column). For this treatment  
26 time,  $T_{\text{Gas}}$  and  $T_{\text{Plate}}$  are still relatively low to induce a thermal desorption (see figure 6) and, thus, the role  
27 on bibenzyl removal of Ar metastables,  $\text{O}(3p^5P)$  and other oxidative species (hydroxyl and ozone), and ions  
28 ( $\text{N}_4^+$ ,  $\text{Ar}^+$  and  $\text{Ar}_2^+$ , see below) is expected to be more significant. In the case of a floating-potential plate,  
29 it takes at least  $60 \text{ s}$  for the APPJ to start removing the bibenzyl from the small central spot (figure 8,  
30 deposits D1 and D2, 3<sup>rd</sup> column). Since the  $\text{O}(3p^5P)$  radiative emission intensity is negligible when using a  
31 floating-potential plate (figure 5), and the  $T_{\text{Gas}}$  and  $T_{\text{Plate}}$  are close to  $T_{\text{Room}}$  (see [4] and figure 7), it can be  
32 fairly assumed that, in this case, Ar metastables are involved in the bibenzyl removal from the central spot  
33 observed at  $t_{\text{exp}}=60 \text{ s}$  in figure 8. Note that  $\text{N}_2^+(B)$  is not formed under our experimental conditions because  
34 Ar metastables do not have enough energy to ionize  $\text{N}_2(X)$ , as it is done by He metastables [61]. However,  
35 the formation of other nitrogen ions such as  $\text{N}_4^+$  (and Ar ions such as  $\text{Ar}^+$  and  $\text{Ar}_2^+$ ) is possible [53,55]. Such  
36 ions can contribute to the formation of the ring patterns around the central spot shown in figure 8, as  
37 suggested for  $\text{N}_2^+(B)$  in [62]. Their production, similarly to that of other species studied when analyzing  
38  
39  
40  
41  
42  
43  
44  
45  
46  
47  
48  
49  
50  
51  
52  
53  
54  
55  
56  
57  
58  
59  
60

1  
2  
3 figure 5, should be more significant when using a grounded plate due to a higher power injected into the  
4 plasma. As so, the effect of those ions on the desorption of bibenzyl is expected to be more significant in  
5 the case of a grounded plate.  
6  
7

8 To study the role of electrons in the desorption process,  $n_e$  and  $T_e$  need to be precisely measured in  
9 the gas phase at the close vicinity of the glass target. Note, however, that for the present argon APPJ, Sousa  
10 *et al* [44] measured the temporal evolution of  $n_e$  and  $T_e$  in the case of a floating-potential glass target placed,  
11 as in the present work, at  $z=5$  mm from the tube's nozzle. At  $z=3.6$  mm,  $n_e$  was found to be  $\sim 9 \times 10^{13} \text{ cm}^{-3}$   
12 and  $T_e$  reached values up to 2 eV (100 ns after the peak of  $I_{\text{DBD}}$ ). Those values are expected to be relatively  
13 higher in the case of a grounded plate due to the higher power injected into the plasma. Although  $n_e$  is  
14 relatively high in our system,  $T_e$  should not exceed 5 eV [10,11,45]. Electrons with much higher energies  
15 can also be available (tail of the EEDF), which can remove, dissociate and ionize organic molecules, but,  
16 under our experimental conditions, their number is much lower than that of the low-energy electrons ( $< 5$   
17 eV) and Ar metastables. On the other hand, Ar metastables have fixed internal energies of 11.5 and 11.7  
18 eV (for  $1s_5$  and  $1s_3$ , respectively), which are sufficient for the selective desorption and/or ionization of  
19 organic molecules (such as bibenzyl with an ionization energy (IE) of 8.7-9.1 eV, paracetamol with an IE  
20 of 9.81 eV, and other hydrocarbons with IE between 9 and 11 eV [65]) from different surfaces. Besides,  
21 the electron mass is negligible as compared to that of heavy species, e.g. argon metastables, and, at the  
22 electron energy range expected in our case, removal of deposited molecules from a target by electrons  
23 should be a rare process. Therefore, under our experimental conditions, the role of electrons on the removal  
24 of bibenzyl is not expected to be significant.  
25  
26  
27  
28  
29  
30  
31  
32  
33  
34

35 A fact that should be also discussed is that the deposits of figure 8 are not perfectly homogeneous.  
36 In our case, bibenzyl, which is solid at ambient temperature, was dissolved in methanol allowing for the  
37 preparation of deposits by evaporation as described in [4]. The initial liquid solutions (methanol + bibenzyl)  
38 deposited on the lamellae were well controlled. But some bibenzyl molecules are lost in the evaporation  
39 process of methanol (see dark regions in the untreated deposits of figure 8), which is impossible to be  
40 controlled, and, thus, their loss cannot be avoided. As so, the quantity of the remaining adherent molecules,  
41 albeit similar, is not the same in different deposits. Other deposition methods such as the spin coating  
42 technique were also tried, but the homogeneity of the films was not improved. This issue could affect the  
43 validity of the results of figure 8. Indeed, even if the APPJ was applied in four fairly homogeneous zones  
44 (see dashed yellow circles in D1-D4 of figure 8), it is not possible to perform a direct comparison between  
45 the desorption efficacy obtained under grounded (D3 and D4) and floating-potential glass plate (D1 and  
46 D2) cases. To overcome this issue and be able to demonstrate the influence of the electric potential of the  
47 glass plate on the desorption efficacy of the APPJ, two approaches were considered, and are described in  
48 the next two paragraphs.  
49  
50  
51  
52  
53  
54  
55  
56  
57  
58  
59  
60

1  
2  
3  
4  
5  
6  
7  
8  
9  
10  
11  
12  
13  
14  
15  
16  
17  
18  
19  
20  
21  
22  
23  
24  
25  
26  
27  
28  
29  
30  
31  
32  
33  
34  
35  
36  
37  
38  
39  
40  
41  
42  
43  
44  
45  
46  
47  
48  
49  
50  
51  
52  
53  
54  
55  
56  
57  
58  
59  
60

The first approach refers to the execution of two series of experiments for each plate condition (see figure 8) and the subsequent numerical processing and statistical analysis of the results (figure 9). To achieve that, an image segmentation algorithm was developed to calculate the percentage of the surface of the lamella covered by bibenzyl molecules (%Bibenzyl). Each image was binarized: the pixels above a chosen brightness threshold were colored in white (corresponding to areas covered in bibenzyl), and those below in black (corresponding to the darker background without bibenzyl). The threshold was chosen so that the generated binary images were very good “mimics” of the experimental images recorded with the stereomicroscope. The %Bibenzyl is then simply the proportion of white pixels. A typical example of the application of this method, referring to deposits D3 and D4 of figure 8, plasma-treated for 60 s in a grounded glass plate, is given in the left frame of figure 9. The photos on the left column depict high-definition images (2058×1536 pixels) of those deposits taken with the stereomicroscope (experimental images). The right column gives the digitized versions of those images after processing with the segmentation algorithm. As it can be seen, an accurate reproduction of the areas of the lamella surface covered by bibenzyl (white color in the right images) is achieved with this approach. Applying this method to the images of the deposits shown in figure 8, the graph of the right frame of figure 9 is obtained. It represents the %Bibenzyl (average value  $\pm$  standard deviation for floating-potential (D1 and D2) and grounded (D3 and D4) glass plates) that is removed from the lamella surface as a function of the plasma treatment time, being the reference the initial quantity of Bibenzyl deposited on the corresponding untreated samples. The first data point ( $t=0$ ) corresponds to the untreated deposits (i.e. the maximum quantity of Bibenzyl deposited on the lamella surface). Note also that, in the case of a grounded glass plate, the treatment time of 10 s refers to only one series of experiments (D4, see figure 8), and, thus, the error given in this case is only the estimated error of the image processing method used. A good reproducibility of the results is obtained for both electric potential conditions of the glass plate. This analysis clearly shows that a higher plasma desorption efficacy is achieved in the case of a grounded plate (black circles) as compared to a floating-potential plate (red circles), validating the differences already revealed by visual inspection of the different deposits shown in figure 8. In conclusion, a more significant bibenzyl removal is achieved under grounded plate conditions.

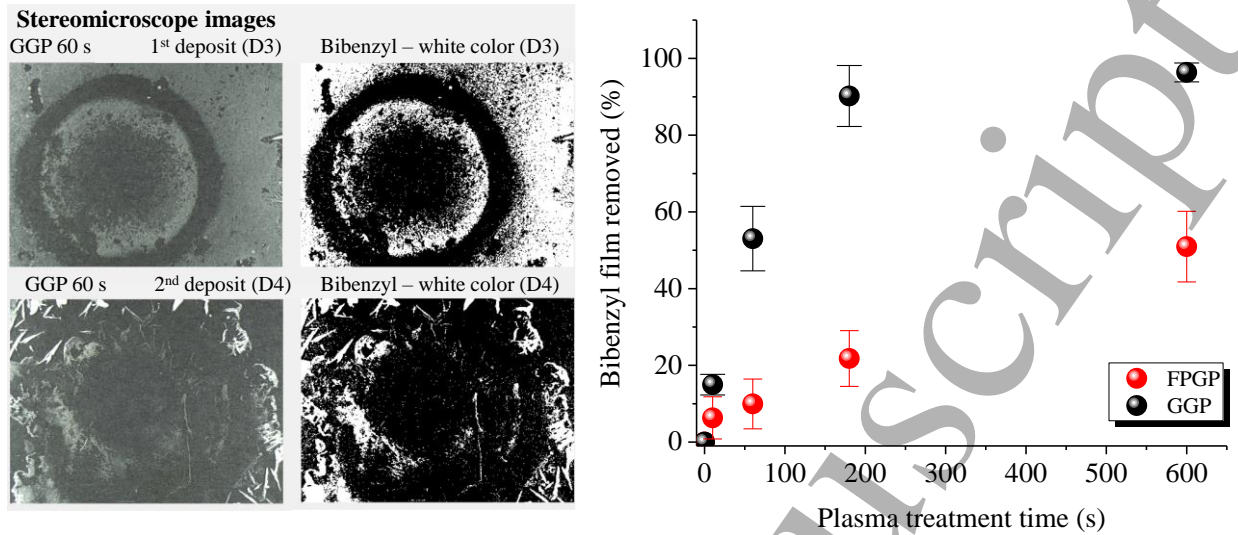


**Figure 9.** *Left frame:* digital processing results (right column) of the experimental images (left column) of the deposits D3 and D4 shown in figure 8 and plasma-treated for 60 s while using a grounded plate (GGP). *Right frame:* Calculated percentage of bibenzyl film removed from the lamella surface as a function of the plasma treatment time for both electric potential conditions of the glass plate (obtained from all deposits of figure 8).

Regarding the second approach, a better validation of the obtained results can be achieved by studying the effect of the APPJ on a much thicker bibenzyl deposit, which is shown in figure 10. For this deposit, bibenzyl molecules directly above the glass are adsorbed to its surface. The bonds between those molecules and the glass surface (adhesion) are most probably much weaker than the bonds formed between the bibenzyl molecules (cohesion). In fact, the application of the argon gas alone (i.e. without plasma), which had a small effect on thin deposits, produces no effect on the thick deposit of figure 10. As so, in the areas where the deposit is thicker, the removal by the plasma treatment of bibenzyl can be initially considered as a de-cohesion of bibenzyl molecules and, in the final layer, as a desorption. In figure 10, the thick deposit was ~10 mm long, ~5 mm wide and ~1–2 mm thick (thinner at its center and thicker at its edges, again due to evaporation issues). The untreated deposit is given in figure 10(a), in which, the dashed red circular zones indicate the different positions of the dielectric tube during the plasma treatment, being their diameter the same as that of the tube. According to the results of figures 8 and 9, the effect of the APPJ on a bibenzyl deposit when using a floating-potential plate should be less significant. This was studied extensively in figure 10 ((b1) to (b4)), by applying the APPJ on different areas of the thick deposit for different times with the glass plate at a floating-potential. Initially, the plasma was applied for 1 min to the middle of the deposit (see circle 1 in figure 10(a)), where it was thinner, being its thickness closer (as much as possible) to that of the deposits of figures 8 and 9. The obtained results are shown in figure 10(b1). Compared to the untreated sample (figure 10(a)), only a small desorption efficacy is observed in the 1<sup>st</sup> treated zone, corresponding to the small hole seen on the deposit in figure 10(b1). However, by applying

1  
2  
3 the APPJ for another 3 min to the same zone, the desorption efficacy increases, i.e. a visible hole  
4 (area $\approx 1.5\times 1.5=2.25\text{ mm}^2$ ) is formed on the deposit (see figure 10(b2)). This result is in relatively good  
5 agreement with those presented in figures 8 (upper frame) and 9 (red curves), where the desorption efficacy  
6 increases with increasing  $t_{exp}$ . Then, the plasma was applied to a 2<sup>nd</sup> zone (circle 2 in figure 10(a)), where  
7 the deposit was relatively thicker compared to the 1<sup>st</sup> zone, and, thus, more difficult to be desorbed. For this  
8 reason,  $t_{exp}$  was increased to 6 minutes. The result is shown in figure 10(b3). It reveals that the APPJ induces  
9 a slow desorption of the bibenzyl molecules from this thick region of the deposit (a second hole with an  
10 area of  $\sim 1.2\times 1.2=1.44\text{ mm}^2$  is observed). Even if the plasma treatment was 50% longer, this desorbed area  
11 is smaller than that of the 1<sup>st</sup> zone because the deposit is thicker in this zone being, thus, the desorption of  
12 bibenzyl more difficult. To investigate if the desorption efficacy on a thick deposit zone also increases with  
13  $t_{exp}$ , the APPJ was applied to a 3<sup>rd</sup> and a 4<sup>th</sup> zones (circles 3 and 4 in figure 10(a), respectively) for 10 and  
14 30 minutes, respectively. The corresponding results are given in figures 10(b3) and 10(b4), respectively.  
15 Based on these images, the areas of the 3<sup>rd</sup> and 4<sup>th</sup> holes are of  $\sim 1.3\times 1.5=1.95\text{ mm}^2$  and  $\sim 2\times 2=4\text{ mm}^2$ ,  
16 respectively. Therefore, compared to the area of the 2<sup>nd</sup> hole (figure 10(b3)), those of the 3<sup>rd</sup> and the 4<sup>th</sup>  
17 holes are  $\sim 1.35$  and  $\sim 2.8$  times larger, and, thus, the desorption efficacy increases with the plasma treatment  
18 time. Note also that the color of the deposit in figures 10(b1)–10(b4) changes progressively from light grey  
19 to yellowish. This is probably due to a greater oxidation activity with increasing  $t_{exp}$ , possibly due to a higher  
20 surface (or volume) density of oxidative species produced by the APPJ or the longer time of interaction  
21 between those species and the bibenzyl molecules [2]. Finally, for comparative purposes, the APPJ was  
22 applied for 30 minutes to a 5<sup>th</sup> thick zone of the same deposit, while using a grounded plate (circle 5 in  
23 figure 10(a)). The obtained results are given in figure 10(c), validating the differences on the plasma  
24 desorption efficacy between using a floating-potential and a grounded plate shown in figures 8 and 9. Note  
25 that the “untreated” deposit of figure 10(c) is that shown in figure 10(b4). In fact, considering the issues  
26 imposed by the inhomogeneities on the comparison of the deposits of figure 8, we used the same thick  
27 bibenzyl deposit to further study the different effect of the APPJ on the removal of bibenzyl between using  
28 a grounded and a floating-potential glass plate. As it can be seen in figure 10, for the floating-potential  
29 plate, even after 50 min of total plasma treatment (i.e. from figures 10(b1) to 10(b4)), the deposit has still  
30 remained unbroken. It has small holes only around the treatment spot and its color changed slowly (not  
31 everywhere) from light grey to yellowish due to the effect of the APPJ. However, when the plate was  
32 grounded (figure 10(c)), by applying the plasma for a much lower time of 30 min (60% of the treatment  
33 time used for the floating-potential plate), a much more significant removal of the thick bibenzyl deposit  
34 was recorded. In this case, a larger bibenzyl removal is observed, not only around the treatment spot (5<sup>th</sup>  
35 treated zone in figure 10(a)), but also in areas that are relatively far from that spot (some of them are  
36 indicated with white lines in figure 10(c)). Furthermore, the color of the deposit i) around the 5<sup>th</sup> treated  
37  
38  
39  
40  
41  
42  
43  
44  
45  
46  
47  
48  
49  
50  
51  
52  
53  
54  
55  
56  
57  
58  
59  
60

1  
2  
3 zone, ii) along its right side and iii) along its inner left side changed drastically from yellowish to dark  
4 brown. Again, this is indicative of a greater oxidation of the deposit when using a grounded plate, in  
5 agreement with the production of oxidative species and ions that is expected to be higher in this case (as it  
6 can be deduced from figure 5). Moreover, among other factors, heating effects can also play a role when  
7 using a grounded plate (see figures 3, 6 and 7), due to the higher power injected into the plasma as compared  
8 to that of a floating-potential plate. The increase of the gas and plate temperatures resulting from the  
9 grounding of the plate seems to induce a melting of the deposit (particularly around the 5<sup>th</sup> treated zone), as  
10 suggested by the drastic change of its color (much darker brown). Thermal effects should also be  
11 responsible for the breaking of the deposit in two parts, as indicated by the yellow dashed lines in figure  
12 10(c). It should be noted that those two cracks on the deposit begin to form in figure 10(b2), and become  
13 progressively more and more noticeable up to figure 10(b4). However, even after 50 min of total treatment  
14 under floating-potential plate conditions (i.e. from figure 10(b1) to 10(b4)), the deposit has still remained  
15 unbroken. In conclusion, a more drastic plasma treatment and a much faster desorption of thin (figures 8  
16 and 9) and thick (figure 10) bibenzyl deposits is achieved when using a grounded plate.

17  
18  
19  
20  
21  
22  
23  
24  
25  
26 Thermal desorption is a technique usually applied to contaminated soils in order to volatilize  
27 hydrocarbons, which are then carried away by a sweep gas or vacuum and eventually destroyed via  
28 incineration or carbon adsorption. Thermal desorption of hydrocarbons can be divided into low-temperature  
29 thermal desorption (LTD, 100–300 °C) and high-temperature thermal desorption (300–550 °C) [63,64].  
30 The gas temperature measured in our case when using a grounded plate ( $92\pm 50$  °C) is close to the lower  
31 limit of temperatures required for LTD. Note also that the melting point of bibenzyl is  $\sim 52$  °C [65], i.e.  
32 within the range of temperatures measured at the impact spot of the plasma on the surface of the glass plate  
33 when it is grounded ( $63\pm 13$  °C). This agrees with the results shown in figure 10(c), where the thick deposit  
34 (treated for 30 minutes) obtains a dark brown color and it seems to be molten around the 5<sup>th</sup> treated zone,  
35 probably due to the non-negligible heating effects after this long treatment time. On the other hand, the  
36 boiling and sublimation points of bibenzyl at atmospheric pressure are both  $\sim 284$  °C [65], which is a much  
37 higher temperature than those measured for the gas and the glass plate even when grounded. Therefore,  
38 taking into account the above information, it is reasonable to assume that bibenzyl can also be removed due  
39 to an LTD process when using a grounded plate (besides the action of the other physicochemical factors  
40 already mentioned). On the contrary, when using a floating-potential plate, its temperature is lower than 30  
41 °C (see reference [4] and figures 3 and 7). Therefore, thermal effects are excluded in this case, and the  
42 observed removal is only due to the action of plasma species such as argon metastables, oxidative species  
43 and ions, resulting in a less significant desorption than in the case of a grounded plate.  
44  
45  
46  
47  
48  
49  
50  
51  
52  
53  
54  
55  
56  
57  
58  
59  
60

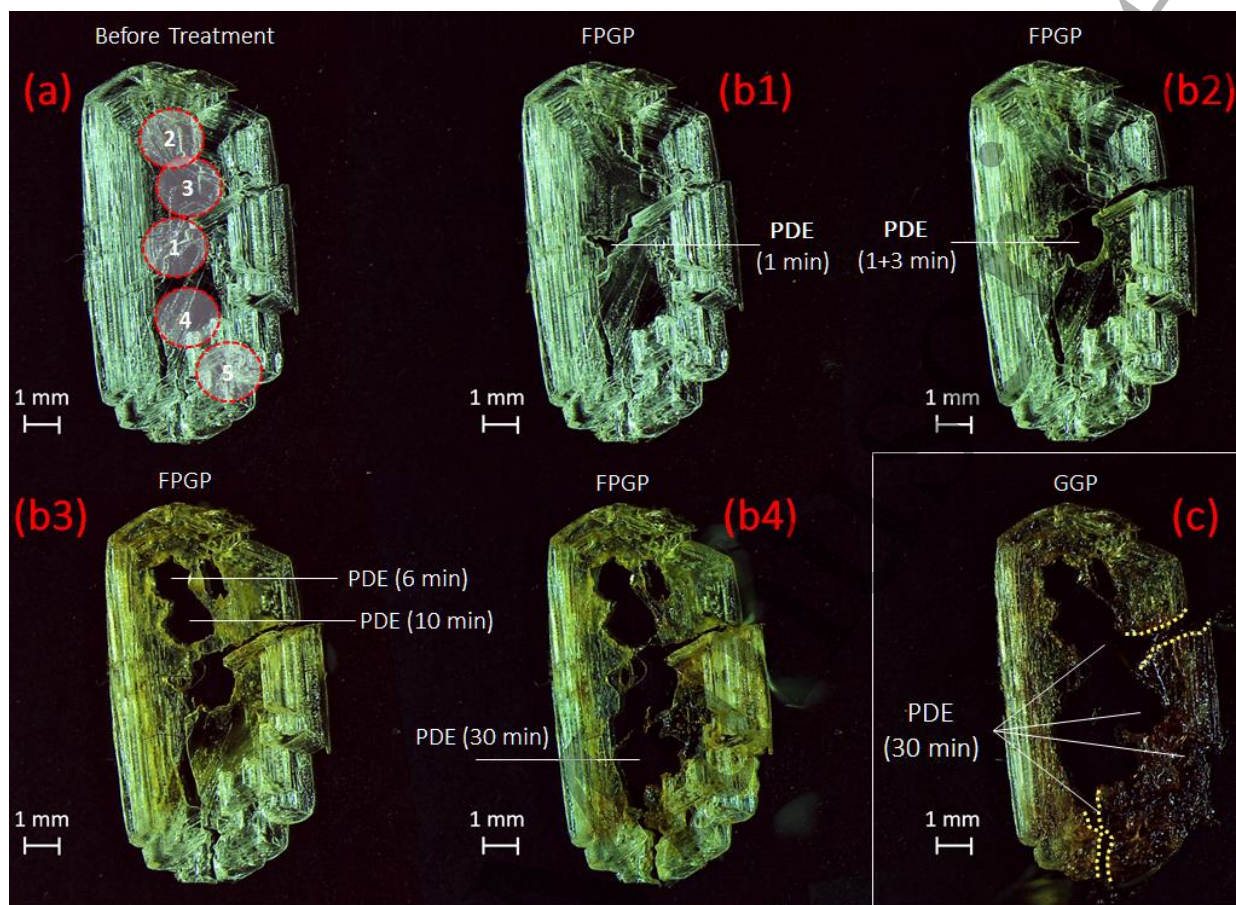


**Figure 10.** High-resolution true-color stereomicroscope images showing the structural modification of a thick bibenzyl deposit after its exposure to the APPJ under floating-potential (FPGP, (b1)–(b4)) and grounded (GGP, (c)) electric potential conditions of the glass plate. (b) FPGP case: plasma applied (b1) for 1 min, and, then, (b2) for another 3 min at the 1<sup>st</sup> treated zone (i.e. circle 1 in (a)), (b3) for 6 min at the 2<sup>nd</sup> zone (circle 2 in (a)), (b3) for 10 min at the 3<sup>rd</sup> zone (circle 3 in (a)) and (b4) for 30 min at the 4<sup>th</sup> zone (circle 4 in (a)). (c) GGP case: plasma applied for 30 min at the 5<sup>th</sup> treated zone (circle 5 in (a)). PDE: Plasma desorption efficacy.

Finally, the developed study in this work can be applicable and effective for the desorption of different substances from various substrates. Besides bibenzyl, many other chemical compounds were studied in the literature [1,30–32,66]. For instance, in [1], a feasibility study is reported on the application of an LTP-MS method for the trace detection of multiclass explosives. The sensitivity and specificity of the method were assayed for several explosives and explosives-related compounds including tetryl, HMX, HMTD, 2,4-dinitrotoluene, 1,3-dinitrobenzene, 1,3,5-trinitrobenzene and many others. Furthermore, in [30], LTP-MS was employed for the desorption and the precise detection of three explosives (TNT, RDX and PETN) from solid substrates. Moreover, the efficiency of this method on the detection of drugs such as cocaine and methamphetamine (even from a human finger avoiding electrical shock and thermal damage), chemicals in complex matrices (including stomach contents of a deceased dog and smokeless tobacco),

1  
2  
3 pharmaceuticals (such as hormones, antiparasitic, antibacterial, paracetamol and many others) and  
4 explosives (similar to those mentioned before), has also been shown [31,32,66]. The physico-chemical  
5 processes involved in the desorption of such substances are not yet well known. Thus, more studies are  
6 necessary to investigate the effect of various operational parameters (e.g. electrical excitation, operating  
7 gas (and gas mixtures), electrode geometry, molecules to be detected, etc.). The present study proposes the  
8 use of an argon APPJ driven by a ns-pulsed high voltage allowing for the generation of a reactive plasma  
9 at ambient air conditions. The choice of a pulsed instead of an AC excitation (widely used in LTP-MS  
10 applications [1,30–32,66]) is advantageous, since this excitation has been proven more efficient to produce  
11 reactive plasma species [67]. Furthermore, bibenzyl is chosen as an alternative approach to the explosives  
12 used in [1,30–32]. Bibenzyl is an aromatic chemical compound and, because many explosives contain  
13 aromatic rings, it can be regarded as a model molecule due to the presence of two phenyl groups. In this  
14 work, we did not investigate the plasma desorption efficacy on other organic compounds, which is  
15 something to be done in the near future. However, given the issues that we had with the homogeneity of  
16 the bibenzyl deposits (see figure 8), in order to further ensure the validity of the results presented in figures  
17 8-10, but also to verify that a similar plasma desorption efficacy can be obtained under equivalent plasma  
18 conditions when using molecules other than bibenzyl, we investigated the action of our APPJ on  
19 poly(methyl-methacrylate) (PMMA -  $(C_5O_2H_8)_n$ ) deposited on silicon sheets (not shown here). The use of  
20 PMMA allowed for the preparation of well homogeneous deposits. Those were treated (same treatment  
21 times as the deposits shown in figure 8) under both electric potential conditions of the glass plate. The effect  
22 of the APPJ was clearly higher in the case of a grounded plate for all treatment times. Therefore, a relatively  
23 similar plasma desorption efficacy is expected when using the present system for the detection of substances  
24 other than bibenzyl under equivalent plasma conditions.

#### 39 IV. CONCLUSION

40 A ns-pulsed Ar APPJ was studied for the fast desorption of resistant bibenzyl deposits placed on a glass  
41 plate that was grounded directly. To demonstrate the feasibility of this approach, the results were compared  
42 to those obtained when using a floating-potential glass plate. TDLAS was applied for the precise temporal  
43 mapping (radial) of the Ar( $1s_5$ ) metastable absolute density close to the glass plate. In this way, the role of  
44 those metastables in the desorption process was investigated. The APPJ was further probed by means of  
45 high-definition photography, thermal imaging and high-resolution emission spectroscopy. When using a  
46 floating-potential plate, the maximum radial density of the Ar( $1s_5$ ) at the center of the APPJ was  $2 \times 10^{13}$   
47  $\text{cm}^{-3}$ . This value was ~17% lower in the case of a grounded plate which can be considered as a small  
48 difference, not significant, since the absorption signal with a grounded plate exhibited 33% higher  
49 fluctuation. Instead, the Ar( $1s_5$ ) density, in the presence of a grounded plate, was noticeably higher in the  
50  
51  
52  
53  
54  
55  
56  
57  
58  
59  
60

temporal range 250–1000 ns after the maximum of the DBD conduction current, being well correlated with the corresponding total plasma emission. Furthermore, the profile of the maximum radial density of Ar( $1s_5$ ) was slightly wider for a grounded plate. Based on the study of emission spectra in the UV-NIR range, it was inferred that the Ar( $1s_5$ ) production through the radiative de-excitation of various 2p levels of excited argon, and its collisional quenching with N<sub>2</sub> giving N<sub>2</sub>(C) (energy transfer reaction), should be more significant for a grounded plate. Assuming that the Ar( $1s_5$ ) losses are the same between floating-potential and grounded plate conditions, the production of Ar( $1s_5$ ) in the residual channel of the streamers should be higher in the case of a grounded plate. Besides, the wavelength-integrated emission of the APPJ and that of the surface ionization wave (developed immediately after the strike of the streamers on the glass plate) were found brighter for a grounded plate. This was probably due to the establishment of a higher axial electric field and electron density, leading to a more conductive channel after the passage of the streamers (a higher current was dragged by the APPJ indeed).

Finally, the plasma desorption efficacy was well demonstrated both on thin and thick bibenzyl deposits. For both electric potential conditions (floating-potential and grounded plate), the desorption efficacy depended on the exposure time to the APPJ, but it was much higher and faster for a grounded plate. The bibenzyl removal was attributed to a combined action of Ar( $1s_5$ ) metastables with oxidative species (such as the atomic oxygen, hydroxyl radical and ozone) and ions (such as N<sub>4</sub><sup>+</sup>, Ar<sup>+</sup> and Ar<sub>2</sub><sup>+</sup>). A closer inspection of the plasma-treated deposits revealed the formation of concentric ring patterns. Such rings should result from a temporal superposition of filamentary streamers that propagate fast on the target. Thermal effects might also play a synergistic role but only in the case of a grounded plate. Indeed, the temperatures of the gas, the quartz tube and the glass plate were significantly higher when using a grounded plate, due to the higher deposited energy in the plasma. The present APPJ can be, therefore, adopted in various fields related to the fast desorption of weakly volatile organic compounds from different surfaces. Besides, a relatively similar plasma desorption efficacy is expected when using the present system for the desorption of substances other than bibenzyl under equivalent plasma conditions. Particularly, its joint use with mass spectrometry (e.g. detection of prohibited substances such as explosives and drugs) seems to be very promising for public-security applications.

## ACKNOWLEDGMENTS

Authors are grateful to M. Odhisea Gazeli (PhD Candidate – Department of Electrical and Computer Engineering, University of Cyprus, Nicosia, Cyprus) for the digital analysis of the deposit images of figure 8. This work was supported by the French “Agence Nationale de la Recherche” (ANR) through the PLASPAMS project (grant N° ANR-2013-SECU-0002-03).

## REFERENCES

- [1] Garcia-Reyes J F, Harper J, Salazar G, Charipar N, Ouyang Z and Cooks R 2011 *Anal. Chem.* **83** 1084
- [2] Damany X, Pasquiers S, Blin-Simiand N, Bauville G, Bournonville B, Fleury M, Jeanney P and J. Santos Sousa 2016 *Eur. Phys. J. Appl. Phys.* **75** 24713
- [3] Fanelli F and Fracassi F 2017 *Surf. Coatings Technol.* **322** 174
- [4] Gazeli K, Vazquez T, Al-Homsi S, Bauville G, Blin-Simiand N, Bournonville B, Fleury M, Jeanney P, Neveu P, Pasquiers S and J. Santos Sousa 2018 *Plasma Process. Polym.* **15** e1800080
- [5] Ricci Castro A H, Kodaira F V P, Prysiashnyi V, Mota R P and Kostov K G 2016 *Surf. Coatings Technol.* **312** 13.
- [6] Puač N, Gherardi M and Shiratani M 2018 *Plasma Process. Polym.* **15** 2
- [7] Tanaka H, Ishikawa K, Mizuno M, Toyokuni S, Kajiyama H, Kikkawa F, Metelmann H-R and Hori M 2017 *Rev. Mod. Plasma Phys.* **1** 3
- [8] Zaplotnik R, Bišćan M, Popović D, Mozetič M and Milošević S 2016 *Plasma Sources Sci. Technol.* **25** 035023
- [9] Darny T, Povesle J M, Puech V, Douat C, Dozias S and Robert E 2017 *Plasma Sources Sci. Technol.* **26** 045008
- [10] Klarenaar B L M, Guaitella O, Engeln R and Sobota A 2018 *Plasma Sources Sci. Technol.* **27** 085004
- [11] Norberg S A, Johnsen E and Kushner M J 2015 *J. Appl. Phys.* **118** 013301
- [12] Yue Y, Pei X, Gidon D, Wu F, Wu S and Lu X 2018 *Plasma Sources Sci. Technol.* **27** 064001
- [13] Abuzairi T, Okada M, Bhattacharjee S and Nagatsu M 2016 *Appl. Surf. Sci.* **390** 489
- [14] Viegas P, Slikboer E, Obrusnik A, Bonaventura Z, Sobota A, Garcia-Caurel E, Guaitella O and Bourdon A 2018 *Plasma Sources Sci. Technol.* **27** 094002
- [15] Lazarou C, Anastassiou C, Topala I, Chiper A S, Mihaila I, Pohoata V and Georghiou G E 2018 *Plasma Sources Sci. Technol.* **27** 105007
- [16] Boeuf J P, Yang L L and Pitchford L C 2013 *J. Phys. D: Appl. Phys.* **46** 015201
- [17] Lu X, Naidis G V, Laroussi M and Ostrikov K *Phys. Rep.* **540** 123
- [18] Babaeva N Yu, Naidis G V, Panov V A, Wang R, Zhao Y and Shao T 2018 *Phys. Plasmas* **25** 063507
- [19] Acsente T, Ionita M D, Teodorescu M, Marascu V and Dinescu G 2016 *Thin Solid Films* **614** 25
- [20] Sarani A, Nikiforov A Y, De Geyter N, Morent R and Leys C *Appl. Surf. Sci.* **257** 8737
- [21] Kostov K G, Nishime T M C, Castro A H R, Toth A and Hein L R O 2014 *Appl. Surf. Sci.* **314** 367
- [22] Van Deynse A, Cools P, Leys C, De Geyter N and Morent R 2015 *Appl. Surf. Sci.* **328** 269
- [23] Wang R, Xu H, Zhao Y, Zhu W, Zhang C, Cheng X and Shao T 2019 *Plasma Chem. Plasma Process.* **39** 187
- [24] Brahme A, Chang Z, Zhao N, Santosh V S, Kondeti K and Bruggeman P J 2018 *J. Phys. D.: Appl. Phys.* **51**, 414002
- [25] Yatom S, Luo Y, Xiong Q and Bruggeman P J 2017 *J. Phys. D Appl. Phys.* **50** 415204
- [26] Yambe K and Abe S 2018 *Plasma Medicine* **8**(1) 23
- [27] Gazeli K, Bauville G, Fleury M, Jeanney P, Neveu O, Pasquiers S and Santos Sousa J 2018 *Plasma Sources Sci. Technol.* **27** 065003
- [28] Niermann B, Reuter R, Kuschel T, Benedikt J, Böke M and Winter J 2012 *Plasma Sources Sci. Technol.* **21** 034002
- [29] Lu X, Naidis G V, Laroussi M, Reuter S, Graves D B and Ostrikov K 2016 *Phys. Rep.* **630** 1
- [30] Zhang Y, Ma X, Zhang S, Yang C, Ouyang Z and Zhang X 2009 *Analyst* **134** 176
- [31] Harper J D, Charipar N A, Mulligan C C, Zhang X, Cooks R G and Ouyang Z 2008 *Anal. Chem.* **80** 9097-9104
- [32] Wiley J S, Shelley J T and Cooks R G 2013 *Anal. Chem.* **85** 14 6545-6552
- [33] Chan G C-Y, Shelley J T, Jackson A U, Wiley J S, Engelhard C, Cooks R G and Hieftje G M 2011 *J. Anal. At. Spectrom.* **26** 1434
- [34] Kind T and Fiehn O 2010 *Bioanal Rev* **2**:23–60
- [35] Kiontke A, Billig S and Birkemeyer C 2018 *Int. j. Anal. Chem.* 5647536 (<https://doi.org/10.1155/2018/5647536>)
- [36] Lindon J, Tranter G E, Koppenaal D, *Encyclopedia of Spectroscopy and Spectrometry*, eBook ISBN:9780128032251
- [37] Niermann B, Böke M, Sadeghi N and Winter J 2010 *Eur. Phys. J. D.* **60** 489
- [38] Sands B L, Leiweke R J and Ganguly B N 2010 *J. Phys. D.: Appl. Phys.* **43** 282001.
- [39] Schmidt-Bleker A, Winter J, Bösel A, Reuter S and Weltmann K D 2016 *Plasma Sources Sci. Technol.* **25** 015005
- [40] Es-sebbar Et, Bauville G, Fleury M, Pasquiers S and Santos Sousa J 2019 *J. Appl. Phys.* **126** 073302
- [41] Shershunova E A, Moshkunov S I, Khomich V yu, 2019 *IEEE Trans. Plasma Sci.* **47** 11 4909
- [42] Sands B L, Huang S K and Ganguly B N 2009 *Appl. Phys. Lett.* **95** 051502

- 1  
2  
3 [43] Yu. P. Raizer, 1991 *Springer-Verlag Berlin Heidelberg* "Gas Discharge Physics", ISBN: 3-540-19462-2  
4 [44] Santos Sousa J, Hübner S, Sobota A, Pasquiers S, Puech V and Sadeghi N 2016 *Proceedings of the 23<sup>rd</sup>*  
5 *ESCAMPIG* Bratislava, Slovakia  
6 [45] Babaeva N, Naidis G V, Panov V A, Wang R, Zhang S, Zhang C and Shao T 2019 *Plasma Sources Sci. Technol.*  
7 **28** 095006  
8 [46] Guaitella O, Marinov I, Pechereau F, Bourdon A and Rousseau A 2011 *Role of adsorbed charges in breakdown*  
9 *and propagation of guided streamer in He 30<sup>th</sup> ICPIG (Belfast, Northern Ireland)* pp 28-30  
10 [47] Dang Van Sung Mussard M, Foucher E and Rousseau A 2015 *J. Phys. D: Appl. Phys.* **48** 424003  
11 [48] Slikboer E, Garcia-Caurel E, Guaitella O and Sobota A 2017 *Plasma Sources Sci. Technol.* **26** 035002  
12 [49] Ji L, Yan W, Xia Y and Liu D 2018 *J. Appl. Phys.* **123** 183302  
13 [50] Yambe K, Kuramoto N and Inagaki Y 2019 *AIP Advances* **9** 085202  
14 [51] Ashpis D E, Laun M C and Griebeler E L 2017 *AIAA J.* **55** 7 (<https://doi.org/10.2514/1.J055816>)  
15 [52] Slikboer E, Sobota A, Guaitella O and Garcia-Caurel E 2018 *J. Phys. D.: Appl. Phys.* **51** 115203  
16 [53] Van Gaens W and Bogaerts A 2013 *J. Phys. D.: Appl. Phys.* **46** 275201  
17 [54] Xiong Q, Nikiforov A Y, Lu X P and Leys C 2010 *J. Phys. D.: Appl. Phys.* **43** 415201  
18 [55] Wu K, Ren C, Jia B, Lin X, Zhao N, Jia P and Li X 2019 *Plasma Process. Polym.* e1900073  
19 [56] Bhatt S, Pulpytel J, Mori S, Mirshahi M, Arefi-Khonsari F, 2014 *Plasma Process. Polym.* **11** 24–36  
20 [57] Prysiazhnyi V, Ricci Castro A H, Kostov K G, 2017 *Braz. J. Phys.* **47** 65–71  
21 [58] Robert E, Darny T, Dozias S, Iseni S and Pouvesle J-M 2015 *Phys. Plasmas* **22** 122007  
22 [59] Douat C, Kacem I, Sadeghi N, Beauville G, Fleury M and Puech V 2016 *J. Phys. D.: Appl. Phys.* **49** 285204  
23 [60] Gazeli K, Svarnas P, Held B, Marlin L and Clément F 2015 *J. Appl. Phys.* **117** 093302  
24 [61] Gazeli K, Thanh Doanh L, Held B and Clément F 2018 *Plasma* **1**, 3  
25 [62] Liu Z, Xu H, Zhou C, Wang W, Liu D and Kong M G 2019 *Plasma Process. Polym.* e1900108  
26 [63] Khan F I, Husain T and Hejazi R 2004 *J. Env. Man.* **71** 95–122  
27 [64] Aggelopoulos C A, Svarnas P, Klapa M I, Tsakiroglou C D 2015 *Chem. Eng. J.* **270** 428-436  
28 [65] The NIST Chemistry WebBook (<https://webbook.nist.gov/cgi/cbook.cgi?Name=bibenzyl&Units=SI>)  
29 [66] Liu Y, Lin Z, Zhang S, Yang C and Zhang X 2009 *Anal. Bioanal. Chem.* **395**:591–599  
30 [67] Walsh J L, Shi J J and Kong M G 2006 *Appl. Phys. Lett.* **88** 171501  
31  
32  
33  
34  
35  
36  
37  
38  
39  
40  
41  
42  
43  
44  
45  
46  
47  
48  
49  
50  
51  
52  
53  
54  
55  
56  
57  
58  
59  
60